



Phase transformation and microwave hydrothermal guided a novel double Z-scheme ternary vanadate heterojunction with highly efficient photocatalytic performance

Debin Zeng^a, Kai Yang^{a,*}, Changlin Yu^{a,b,*}, Fanyun Chen^a, XiaoXiao Li^a, Zhen Wu^a, Hong Liu^{b,**}

^a School of Metallurgy and Chemical Engineering, Jiangxi University of Science and Technology, 86 Hongqi Road, Ganzhou 341000, Jiangxi, China

^b Key Laboratory for Water Quality and Conservation of the Pearl River Delta, Ministry of Education, Institute of Environmental Research at Greater Bay, Guangzhou University, Guangzhou 510006, Guangdong, China

ARTICLE INFO

Keywords:

Self-phase transition
Double Z-scheme ternary vanadate heterojunction
Microwave hydrothermal
Interface charge transfer
Photocatalysis

ABSTRACT

Semiconductor-based heteronanostructures with the high carriers-flow steering and high activity and stability in the visible-light-driven multicomponent photocatalytic system have been of great concern due to its long-standing demand in the wide application of environmental protection and energy conversion. However, the construction of ternary-component nanocrystals usually undergoes multiple complex steps to restrict its application. In the work, we successfully report the facile design and synthesis of a novel double Z-scheme $\text{Zn}_3(\text{VO}_4)_2/\text{Zn}_2\text{V}_2\text{O}_7/\text{ZnO}$ ternary heteronanostructure system (THS) via self-phase transition with heating on basis of the $\text{Zn}_3(\text{OH})_2\text{V}_2\text{O}_7 \cdot 2\text{H}_2\text{O}$ precursor in a low-cost microwave hydrothermal assistant, which exhibited excellent photocatalytic performances. In this case, the employment of $\text{Zn}_3(\text{OH})_2\text{V}_2\text{O}_7 \cdot 2\text{H}_2\text{O}$ as the heteronanostructure precursor is the key for fabricating the THS material, which not only boosted the interaction with its structure and but also maintained the mesoporous nanosheet structure. It has been proved that $\text{Zn}_3(\text{OH})_2\text{V}_2\text{O}_7 \cdot 2\text{H}_2\text{O}$ firstly lost its H_2O and then the partial $\text{Zn}_3(\text{VO}_4)_2$ underwent the self-phase transition process to produce $\text{Zn}_2\text{V}_2\text{O}_7$ and ZnO ($\text{Zn}_3(\text{OH})_2\text{V}_2\text{O}_7 \cdot 2\text{H}_2\text{O} \rightarrow \text{Zn}_3(\text{VO}_4)_2 \rightarrow \text{Zn}_2\text{V}_2\text{O}_7 + \text{ZnO}$), which obtained the double Z-scheme THS. Accordingly, the interfacial-dominated photocatalysis reactivities such as the removal of phenols and dyes were used as ideal experiments to verify the responsibility of the constructed double Z-scheme THS material that was equipped with the narrow band gap, intimate contact interface, the wide visible light absorption and more efficient charge transfer and separation for high visible-light photocatalytic reactivity and stable cycling. PL spectra, radicals trapping experiments and ESR tests confirmed that the nontraditional transport of photoinduced h^+ and e^- caused by double Z-scheme mechanism played an important role in the efficient removing the target pollutants. Such a synthetic approach maybe render double Z-scheme THS to advance the development for large-scale applications of the hetero-transition metal vanadates.

1. Introduction

Over the past decades, wastewater pollution from a large number of organic pollutants discharged by printing, dyeing, metallurgical and chemical industries becomes a major source of threat to water environmental safety [1,2], which has been an important research hotspot among scientific community [3]. However, as for the persistent organic pollutants (POPs), e.g. phenols 6-hydroxymethyl uracil, dinitrophenol, bisphenol A, it is difficult to eliminate these POPs with conventional water treatment technologies [4–6]. The efficient and eco-friendly semiconductor photocatalytic technology, as an effective solution to settle worldwide energy shortages and environmental purification, has

received intense attention [7,8]. For example, the photocatalytic removals of NO_x [9] and phenols [10] were considered as important research directions to address environmental issues. Upon the irradiation of light ($\geq E_g$), the photocatalysts can produce photogenerated electrons (e^-) and hole (h^+) pairs, where the e^- and h^+ can generate the strong oxidative species of $\cdot\text{O}_2^-$ and $\cdot\text{OH}$ with invigorative ability to destroy and mineralize the organic pollutants into harmless CO_2 and H_2O molecules [11,12].

Up to now, a series of methods were employed to synthesize various photocatalysts, such as TiO_2 [4,13], ZnO [14], WO_3 [15], BiVO_4 [16], CdS [17] and novel silver-based semiconductor (Ag_2CO_3 [18], Ag_3PO_4 [19], AgX ($\text{X} = \text{Cl}, \text{Br}, \text{I}$) [20,21]). Although they are considered as

* Corresponding author at: School of Metallurgy and Chemical Engineering, Jiangxi University of Science and Technology, 86 Hongqi Road, Ganzhou 341000, Jiangxi, China.

** Corresponding authors.

E-mail addresses: yangkai19871006@126.com (K. Yang), yuchanglinjx@163.com (C. Yu), liuhong@gzhu.edu.cn (H. Liu).

efficient and advanced option for photocatalytic degradation of organic pollutants in a certain extent, the further application of those is enslaved to face various defects such as larger bandgap or self-photo-corrosion or low quantum yield or serious recombination of photogenerated e^-/h^+ pairs. As well known, the recombination of e^- and h^+ is in competition with the photocatalytic degradation process, which is generally recognized as a key factor limiting the kinetics of active species transmission and reaction rate. To conquer this limitation, a wide variety of efforts for photocatalysts modification have been proposed, such as the modified methods of non-noble metal doping [22,23] or noble metals deposition [24,25]. Yan et al. [22] designed three-dimensionally ordered macroporous Fe^{3+} doped TiO_2 photocatalysts by Fe^{3+} ions doping as the acceptor/donor center to reduce the bandgap and improve its surface electronic properties and achieve good effect of visible-light-degradation of rhodamine B. Also, the halogen (F, Cl, Br, I) doped $g-C_3N_4$ exhibited more excellent photocatalytic performance because of its wide visible-light-response, narrow bandgap and reducing work function *via* the joint calcinating of ammonium halides and melamine [23].

In the composite semiconductor system, design Z-scheme system can effectively promote the photocatalytic performance. For example, a sandwich-structured sulfur-doped $g-C_3N_4/Au/CdS$ Z-scheme was prepared by two-step self-assembly process. Favoring by the Z-scheme chargecarrier transfer mechanism, the redox ability of photoinduced electron-hole pairs was boosted remarkably [24]. In another graphene-bridged $Ag_3PO_4/Ag/BiVO_4$ Z-scheme photocatalyst, the enhanced photocatalytic performance was obtained. In this $Ag_3PO_4/Ag/BiVO_4$ system, Ag played an important role on receiving photoinduced electrons from $BiVO_4$ and holes from Ag_3PO_4 [25]. In addition, another effective method by constructing heterogeneous junction structure at the interface combined with other semiconductor materials [9,14,18,26,27] could impressively enhance the photoactivity due to the enhanced utilization of sunlight or the high separation/transportation of photogenerated e^-/h^+ pairs. Moreover, constructing novel direct solid-state Z-scheme heterojunction is thought to be more promising route to promote photocatalytic activity. Chen et al. [26] developed a synergistic $GO/Ag_2CrO_4/g-C_3N_4$ double Z-scheme system *via* one-step chemical precipitation. Due to the enhancement of visible-light absorption and nontraditional transport of photoinduced h^+ and e^- caused by double Z-scheme mechanism, the photocatalytic performance and the stability were remarkably enhanced. Hong et al. [27] designed a novel direct solid-state Z-scheme $V_2O_5/g-C_3N_4$ heterojunction *via* a facile *in-situ* growth method. The active species trapping and electron spin resonance (ESR) experiments confirmed that this Z-scheme system not only improved the separation photoinduced electron-hole pairs but also enhanced its ability for organic pollutants purification. These results indicate that tailoring and fabrication of the Z-scheme phase interface/heterojunctions between the light harvesting semiconductors afford a promising route to enhance the photocatalytic efficiencies. However, the studies of the synthetic process in this area are currently unsystematic, and almost all studies reported thus far about heterojunction systems with high efficiency and stability are focused on the coherent superimposition of the heterogeneous photocatalysts by the complicated multistep process.

Different from multi-step synthesis of heterojunction, the one-step phase-transition synthesis possesses fascinating and distinctive superiority, which can provide an important guide on designing unique structure and tight interface among multivariate heterojunction [28–31]. A phase-junction TiO_2 nanocomposites with a tunable ratio of rutile to anatase was successfully developed by phase-transition route. The results confirmed that the synergistic effect between two phase remarkably facilitated the transfer of photon between solid-solid interfaces [32]. A phase-junction of tetragonal and monoclinic $BiVO_4$ nanofibers was successfully constructed by calcination temperature control. The boosted photocatalytic performance under visible light irradiation was attributed to the photon transition between tetragonal

and monoclinic $BiVO_4$ nanofibers [33]. Moreover, based on our previous work, we have also developed a novel and stable Ag_2O/Ag_2CO_3 heterostructured catalyst synthesized by a facile, low-cost, and one-step phase-transition method, where the well-defined junctions between Ag_2O and Ag_2CO_3 could facilitate charge transfer and suppress the recombination of photogenerated carriers with extremely high activity and stability [18]. It indicates that the constructing method through the phase transformation of corresponding thermally unstable semiconductor is an efficient pathway. With these theoretical design and motivations, we herein report the intentional design of double Z-scheme ternary heterojunction system (THS) by a facile method that the high temperature calcination promoted the partial phase transition process of $Zn_3(VO_4)_2$ to predominantly focus on studying the effect of thermal treatment on the photocatalytic performance for efficiently removing organic pollutants over zinc vanadate composites. The structure, composition, optical and electrochemical properties, separation and transport of photogenerated e^-/h^+ pairs and the generation of active radicals were investigated in detail as well, which was mainly focused on how to remove the common phenols in water environment with great harmness for human health [34]. The possible process of the constructed double Z-scheme THS was proposed and it was found that the synergetic effect of the THS greatly overcame the defect of poor visible light response and the high recombination rates of photogenerated e^-/h^+ pairs in single component photocatalyst of pure $Zn_3(VO_4)_2$. It is worth noting that this work provides a constructive guidance for facilely and environmentally developing multivariate heterojunction photocatalyst with visible light response.

2. Experimental

2.1. Synthesis of $Zn_3(VO_4)_2/Zn_2V_2O_7/ZnO$ double Z-scheme ternary heterostructure nanosheets

The chemicals of analytical grade such as $Zn(CH_3COO)_2 \cdot 2H_2O$, NH_4VO_3 , ethanol, rhodamine B, methyl orange, acid orange II, methylene blue, phenol and p-chlorophenol were purchased from Sinopharm Chemical Reagent Co. Ltd. China and used without further purification. Bisphenol A was purchased from Dr. Ehrenstorfer GmbH, Augsburg, Germany.

$Zn_3(OH)_2V_2O_7 \cdot 2H_2O$ precursors were firstly prepared *via* a microwave hydrothermal process. Specially, 3 mmol of $Zn(CH_3COO)_2 \cdot 2H_2O$ and 2 mmol of NH_4VO_3 were dissolved thoroughly in 30 mL of deionized water at room temperature, respectively. The NH_4VO_3 solution was then added dropwise into the $Zn(CH_3COO)_2 \cdot 2H_2O$ solution under magnetic stirring and the pH value was adjusted to 10.0 by NaOH solution of 1 M. After stirring for 2 h, the mixture was transferred into a 100 mL Teflon reaction kettle and the reaction kettle was placed in a microwave hydrothermal instrument, which was heated to 160 °C for 30 min. After the solution was cooled down to room temperature, the precursors of white precipitates were collected, washed with ethanol and distilled water for three times, and dried at 60 °C for 10 h to obtain $Zn_3(OH)_2V_2O_7 \cdot 2H_2O$.

Secondly, the obtained $Zn_3(OH)_2V_2O_7 \cdot 2H_2O$ precursors were placed in a muffle furnace and calcinated at 400, 500, 600, 700 and 800 °C for 2 h, respectively. And also, the samples were denoted as S-400, S-500, S-600, S-700 and S-800. The uncalcinating sample was named as S-U. For further comparsion, a sample from $Zn_3(OH)_2V_2O_7 \cdot 2H_2O$ precursors by precipitation assistant process was prepared, which was calcinated at 700 °C and denoted as P-700.

2.2. Characterization

Powder X-ray diffraction (XRD) patterns were recorded at a scanning rate of 0.05°/s by X-ray diffractometer (Bruker D8, advance) with Cu K α ($\lambda = 0.15418$ nm), where the test voltage was 40 kV and the applied current was 40 mA. Thermogravimetric analysis (TGA) and

differential thermal analysis (DTA) and differential scanning calorimetry (DSC) were performed on a NETZSCH STA 449F5 Thermal Analyzer at a heating rate of 30 °C/min in N₂ flow. Scanning electron microscopy (SEM) of samples was measured on an instrument (FLA650F, FEI company in the United States). Transmission electron microscopy (TEM) and high-resolution transmission electron microscopy (HRTEM) images were recorded on a JEOL JEM-2010FEF Field Emission Electron Microscope. The Brunauer–Emmett–Teller (BET) surface areas of samples were collected from N₂ adsorption/desorption isotherms by liquid nitrogen at 77 K on an automatic analyzer (ASAP 2020), which were outgassed for 2 h under vacuum at 120 °C prior to adsorption. UV–vis diffuse reflectance spectra (DRS) were obtained from UV–vis spectrophotometer (UV-2550, Shimadzu) by BaSO₄ as the reflectance sample. Fourier transform infrared (FT-IR) spectra were recorded with a Nicolet 5700 FT-IR spectrometer, where the samples were pressed by a KBr disk preparation apparatus. Raman spectra were recorded on an in Via-Reflex Raman microprobe with 514 nm laser excitation. X-ray photoelectron spectroscopy (XPS) measurements were determined by a PHI Quantum 2000 XPS system with a monochromatic Al K α source and a charge neutralizer and all the binding energies were referenced to the characteristic of C1s peak at 284.8 eV. The photoluminescence (PL) emission spectra of samples were executed by a fluorescence spectrometer (Hitachi F-4500, Japan) using an excitation wavelength of 325 nm. The electron spin resonance (ESR) spectra were obtained from an electron spin resonance spectrometer (Bruker ER200-SLC, Germany), where 5, 5-dimethyl-1-pyrroline N-oxide (DMPO: 50 mM, 0.2 mL) was used as the stabilizer of active species in the aqueous with the suspended photocatalyst. The settings of ESR spectrometer were as follows: center field = 323.467 mT, sweep width = 5 mT, microwave frequency = 9069 MHz, and microwave power = 0.998 mW. Photoelectrochemical measurements were performed by a conventional three-electrode quartz cell in an electrochemical workstation (CHI-660E, China). The saturated Ag/AgCl and platinum wires were utilized as reference electrode and the counter electrode, respectively. 0.1 M of Na₂SO₄ solution (pH = 6.8) was used as electrolyte solution. The working electrode was used as the drop-coating method on indium tin oxide (ITO) conducting glass. The preparation of the working electrodes follows as the following method: the slurry of 1 mL ethanol and 10 mg samples was spread onto ITO with the area of 1 cm². After air drying, the working electrode was further dried at 60 °C for 2 h to improve adhesion. A xenon lamp (CEL-HXF300) without a cutoff filter was used to provide the simulated sunlight light for photocurrent test.

2.3. Photocatalytic activity

The photocatalytic experiments were tested by a photochemical reactor. For degradation experiments of Rhodamine B, Methyl orange, Acid orange II and Methylene blue, 30 mg of photocatalyst was suspended on the aqueous solution of the above organic dyes (50 mL, 10 mg/L). A 400 W metal halide lamp (95% of ≥ 420 nm visible light and 5% ultraviolet light) was applied to simulate sunlight source. Prior to irradiation, the suspension was magnetically stirred in the dark for 40 min to achieve the adsorption and desorption equilibrium of organic dyes on the catalysts. The reactor system was maintained at room temperature (ca. 20 °C) by circulating cooled water. Approximately, 2 mL of suspension was sampled at given time intervals under light irradiation and centrifuged to remove photocatalyst powders. The upper layer filtrates were drew for further analysis by a UV–vis spectrophotometer. The procedure for the degradation of phenol (10 mg/L), 4-chlorophenol (10 mg/L) and bisphenol A (10 mg/L) were carried out on 500 W xenon lamp (Solar-500N) and other processes were the same as that described above. The removal ratios (R) and of pollutants were determined as follows:

$$R = (1 - C/C_0) \times 100\% \quad (1)$$

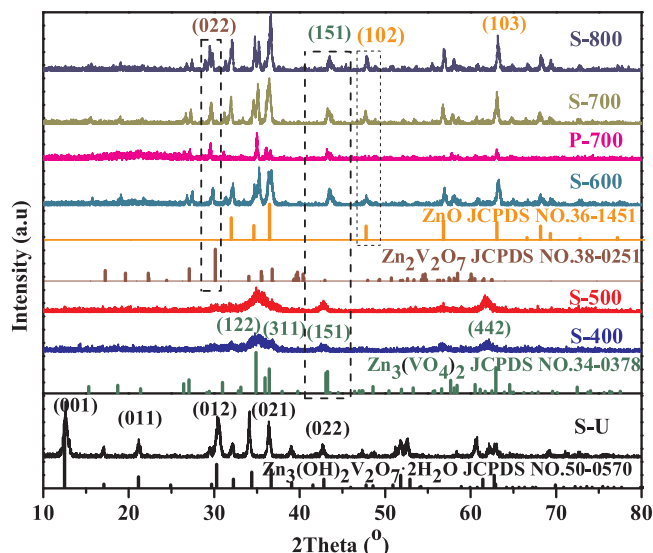


Fig. 1. XRD patterns of Zn₃(OH)₂V₂O₇·2H₂O and the samples calcinated at different temperatures.

Where C_0 and C are the initial concentration of pollutant, and its concentration at given irradiating time intervals, respectively. The removal ratio of total organic carbon (TOC) was measured with a vario TOC analyzer (Vario TOC, German Elementar Company).

3. Results and discussion

3.1. Phase structure

The phase structures and crystallinities of the samples prepared at different conditions were investigated by powder X-ray diffraction (XRD) patterns. As shown in XRD patterns of Fig. 1, it can be clearly observed that the characteristic diffraction peaks of unroasted sample at 2θ of 12.6°, 21.1°, 30.2°, 36.4° and 43.5° are assigned to (001), (011), (012), (021) and (022) crystal planes of hexagonal Zn₃(OH)₂V₂O₇·2H₂O (JCPDS No.50-0570), respectively. And also, no other impurity phase can be found. As observed over S-400 and S-500, it can be confirmed that the characteristic diffraction peaks at 2θ of 34.9°, 36.4°, 43.5° and 61.8° are ascribed to (122), (311), (151) and (442) crystal planes of orthorhombic Zn₃(VO₄)₂ (JCPDS No. 34-0378), respectively. The intensity of the diffraction peak observed in S-500 becomes sharper than that of S-400, indicating the improving crystallinity. Interestingly, as the increase of roasting temperature (> 500 °C), following by a phase transformation process on partial Zn₃(VO₄)₂, new characteristic diffraction peaks appear on the samples of higher temperature. The new characteristic diffraction peaks appear at 2θ of 17.2°, 22.3°, 29.8° and 36.7°, in agreement with standard peaks of monoclinic Zn₂V₂O₇ (JCPDS No. 38-0251). And meanwhile, it is obvious that the 2θ peaks of 31.8°, 36.5°, 47.6°, 56.8° and 63.3° are corresponding to the standard peaks of hexagonal ZnO (JCPDS No. 36-1451). From the above XRD analyses, as a partial of Zn₃(VO₄)₂ undergoing phase transition process to produce Zn₂V₂O₇ and ZnO phases at higher temperature (Zn₃(OH)₂V₂O₇·2H₂O → Zn₃(VO₄)₂ → Zn₂V₂O₇ + ZnO), the heating of Zn₃(OH)₂V₂O₇·2H₂O of 600 °C with a time of 2 h can result in the formation of ternary Zn₃(VO₄)₂/Zn₂V₂O₇/ZnO heterojunction, strongly suggesting that the heating temperature played an important role in the formation of heterojunction interface in the Zn₃(OH)₂V₂O₇·2H₂O nanosheets. Interestingly, exceeding the higher temperature of 600 °C and lower than 800 °C, Zn₃(VO₄)₂ didn't completely dissolve and the composite system held the state of ternary heterojunction. But no diffraction peaks exist at 2θ of 31.8° and 47.6° over the P-700 sample prepared by precipitation assistant method comparing with S-700 and

Table 1
Average crystallite sizes and specific surface areas of the prepared samples.

Samples	Average crystallite size (nm)	Samples	Average crystallite size (nm)
S-U	19.90	S-400	12.21
S-500	15.63	S-600	16.83
S-700	18.37	S-800	21.83
P-700	37.17		

the most of peaks over P-700 are assigned to that of $\text{Zn}_3(\text{VO}_4)_2$, indicating no definitive formulation of ternary heterojunction.

The average grain sizes of the samples obtained by different roasting temperatures were estimated through the Scherrer equation of $D = K\lambda/(\beta \cos \theta)$ as a benchmark of the strongest diffraction peaks. The results as presented in Table 1 display that the average crystallite size increase with the rise of temperature and the sample prepared by precipitation method has a maximum crystallite size.

3.2. Thermal analysis

Thermogravimetric analysis (TGA), derivative thermogravimetry (DTG) and differential scanning calorimetry (DSC) were carried out to reveal the dehydration process of $\text{Zn}_3(\text{OH})_2\text{V}_2\text{O}_7 \cdot 2\text{H}_2\text{O}$ and prove the phase transformation of $\text{Zn}_3(\text{VO}_4)_2$ with the increasing temperature. As shown in Fig. 2, it can be confirmed that there exists a distinct dehydration process by the TG and DTG curves on $\text{Zn}_3(\text{OH})_2\text{V}_2\text{O}_7 \cdot 2\text{H}_2\text{O}$, in which 11.01% of the weight loss on $\text{Zn}_3(\text{OH})_2\text{V}_2\text{O}_7 \cdot 2\text{H}_2\text{O}$ belongs to the evaporation of the adsorbed water and crystalline water below 220 °C ($\text{Zn}_3(\text{OH})_2\text{V}_2\text{O}_7 \cdot 2\text{H}_2\text{O} \rightarrow \text{Zn}_3(\text{OH})_2\text{V}_2\text{O}_7 + 2\text{H}_2\text{O}$). From 220 to 496 °C, a weight loss of about 3.72% (reference to $\text{Zn}_3(\text{OH})_2\text{V}_2\text{O}_7$) can match with the following reaction $\{\text{Zn}_3(\text{OH})_2\text{V}_2\text{O}_7 \rightarrow \text{Zn}_3(\text{VO}_4)_2 + 2\text{H}_2\text{O}\}$ according to mass ratio of H_2O and $\text{Zn}_3(\text{OH})_2\text{V}_2\text{O}_7$ for the dehydration of crystalline water, which is in good agreement with the report [35]. As well known, most of the decomposition reactions are endothermic. It is found that the DSC plot made clear two endothermic peaks at 45–855 °C due to the decomposition of $\text{Zn}_3(\text{OH})_2\text{V}_2\text{O}_7 \cdot 2\text{H}_2\text{O}$. One endothermic process mainly corresponds to the loss of water molecules, interestingly, it is notable that another endothermic process occurs at 496–855 °C and there is no mass loss, suggesting the decomposition reaction of $\text{Zn}_3(\text{VO}_4)_2$. In line with XRD analysis, the decomposition of $\text{Zn}_3(\text{OH})_2\text{V}_2\text{O}_7$ lost its water and a followed part of $\text{Zn}_3(\text{VO}_4)_2$ decomposed into $\text{Zn}_2\text{V}_2\text{O}_7$ and ZnO phases at above 496 °C, constructing the ternary heterojunction with $\text{Zn}_3(\text{VO}_4)_2/\text{Zn}_2\text{V}_2\text{O}_7/\text{ZnO}$. Based on the above data, it can be deduced that the reaction of $\{\text{Zn}_3(\text{OH})_2\text{V}_2\text{O}_7 \cdot 2\text{H}_2\text{O} \rightarrow \text{Zn}_3(\text{VO}_4)_2 + 3\text{H}_2\text{O}\}$ occurs at below 500 °C and the partial decomposed reaction of $\{\text{Zn}_3(\text{VO}_4)_2 \rightarrow \text{Zn}_2\text{V}_2\text{O}_7 + \text{ZnO}\}$

belongs to 600, 700 and 800 °C, which is consistent with the XRD results. Although the thermal decomposition reactions of $\text{Zn}_3(\text{OH})_2\text{V}_2\text{O}_7 \cdot 2\text{H}_2\text{O}$ and $\text{Zn}_3(\text{VO}_4)_2$ are fairly complex kinetic process, it expects to obtain the stable and excellent $\text{Zn}_3(\text{VO}_4)_2/\text{Zn}_2\text{V}_2\text{O}_7/\text{ZnO}$ heterojunction phases by precise control of the calcining temperature and time.

3.3. Morphologic structure

The morphology structures and the close ternary heterojunction of the as-prepared samples were investigated by SEM and TEM methods. Fig. 3(a) and (b) indicates that the S-U $\{\text{Zn}_3(\text{OH})_2\text{V}_2\text{O}_7 \cdot 2\text{H}_2\text{O}\}$ and S-500 $\{\text{Zn}_3(\text{VO}_4)_2\}$ are composed of the regular and smooth nanosheet structures, whose diameters range from 0.3 to 0.8 μm and the thickness is about 50 to 100 nm. It makes clear that the hierarchical nanosheets of S-500 as presented by Fig. 3(c) and (d) show no change for overall morphologies comparing with the S-U, indicating that the S-U only done the dehydration of the adsorbed water and crystalline water at below 500 °C. Fig. 3(e)–(h) demonstrates the distinct changes in the morphologies. And also, direct heating of $\text{Zn}_3(\text{VO}_4)_2$ nanosheets at the temperature of 700 °C for 2 h in air not only resulted in the phase transformation of partial $\text{Zn}_3(\text{VO}_4)_2$, but also brought on numerous small nanosheets with a diameter range from 20 to 50 nm on their surfaces. Importantly, HRTEM image in Fig. 3(i) further confirms that there are the presence of ternary $\text{Zn}_3(\text{VO}_4)_2/\text{Zn}_2\text{V}_2\text{O}_7/\text{ZnO}$ heterostructures produced by phase transformation of partial $\text{Zn}_3(\text{VO}_4)_2$. It is evident that there are three sets of distinct lattice fringes, in which the interplanar spacings of 0.257, 0.311 and 0.248 nm correspond well to the crystal plane of (122) in $\text{Zn}_3(\text{VO}_4)_2$ (JCPDS No.34-0378), the crystal plane of (022) in $\text{Zn}_2\text{V}_2\text{O}_7$ (JCPDS No. 38-0251) and the crystal plane of (101) in ZnO (JCPDS No. 36-1451), respectively. The obtained ternary nanosheets materials with close contact can well build up the photocatalytic properties.

For the further confirmation, the elemental mapping image of the heterostructure for the selected area was conducted as shown in Fig. 4(a–e), indicating that the two constituents of Zn and O elements are homogeneously distributed throughout the detected region. And also, it can be seen from the distribution area of the compositional elements of V that larger nanosheets (reddish region in Fig. 4d) are mainly composed of $\text{Zn}_3(\text{VO}_4)_2$ and $\text{Zn}_2\text{V}_2\text{O}_7$ after the calcinating at temperature of 700 °C. But the tiny patches on the surfaces of the composites are mostly made up of ZnO nanoplates, confirming that in the process of the phase transformation of partial $\text{Zn}_3(\text{VO}_4)_2$, the partial decomposed production of ZnO develops along with themselves epitaxial surfaces of vanadate and they can very tightly knit together. And based on this, we inferred a possible process that the epitaxial coating of ZnO for $\text{Zn}_3(\text{VO}_4)_2$ nanosheets therefore prevents the complete thermal decomposition of $\text{Zn}_3(\text{VO}_4)_2$.

3.4. Surface area and pore structure

The pore-size distributions and specific surface areas of the as-synthesised samples were investigated by N_2 adsorption/desorption measurements as displayed in Fig. 5. Meanwhile, the variations of BET surface areas and pore structures can be summarized in Table 2. According to Brunauer-Deming-Deming-Teller (BDDT) classification, all the samples are identified as the type IV and the convex low pressure region implies that there is a strong interaction between nitrogen and materials [36]. All the samples show the large amount of adsorption on the high pressure region, indicating the presence of micropores from the slit-like pores formed by the aggregation of $\text{Zn}_3(\text{VO}_4)_2$ nanosheets. Also, the hysteresis loops belong to type H_3 and H_2 , respectively [37–39]. As shown in inset figure, the pore size distribution curves of the samples in the texture present a wide pore size distribution and the followed enlargement as the increase of the temperature.

The specific surface area, the average pore size and the pore volume

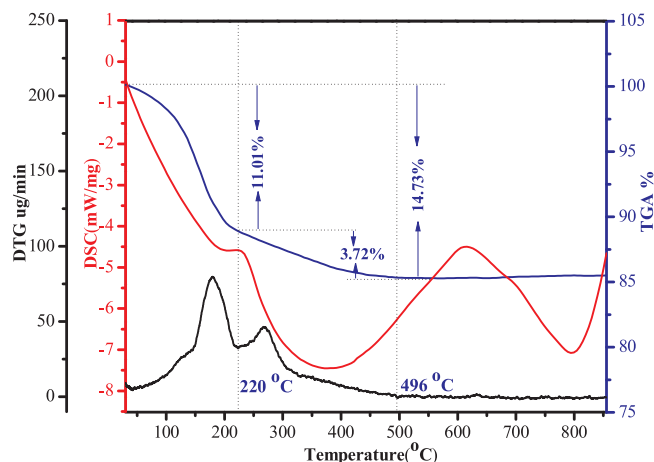


Fig. 2. Thermal analysis of S-U ($\text{Zn}_3(\text{OH})_2\text{V}_2\text{O}_7 \cdot 2\text{H}_2\text{O}$).

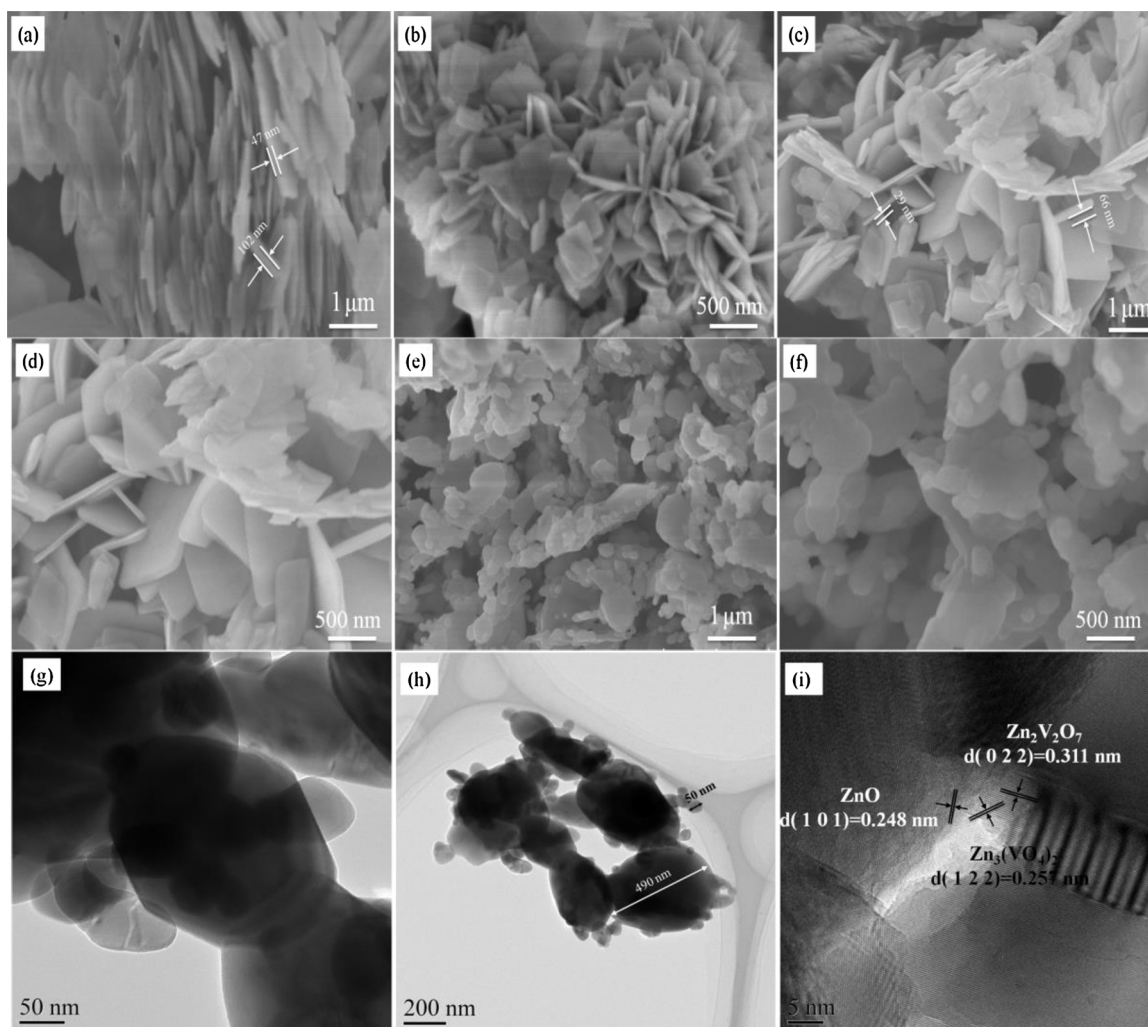


Fig. 3. SEM and TEM images of the typical samples: (a) and (b) represent that of S-U ($\text{Zn}_3(\text{OH})_2\text{V}_2\text{O}_7 \cdot 2\text{H}_2\text{O}$); (c) and (d) represent that of S-500; (e) and (f) represent that of S-700; (g), (h), and (i) represent HRTEM images of S-700.

are displayed in Table 2. As reflected in the data, the specific surface area increases and then decreases with the increase of calcinating temperature, revealing that $\text{Zn}_3(\text{OH})_2\text{V}_2\text{O}_7 \cdot 2\text{H}_2\text{O}$ dehydrates into the $\text{Zn}_3(\text{VO}_4)_2$, in favour of the increase of specific surface area. However, at the higher temperature of 700 °C, the phase transition of partial $\text{Zn}_3(\text{VO}_4)_2$ nanosheets leads to the decrease in the specific surface area, in accordance with SEM analysis, which comes from the aggregation of nanosheets. As is well known, rich porous structures can provide effective transport channel for reactants and product molecules, giving rise to a remarkably enhanced photocatalytic performances [40,41]. Based on average pore sizes of S-U, S-500 and S-700, it can be found that the average pore size gradually decreases and the S-700 has minimum average pore size, indicating that the adsorption of the reactants on the micropores is not the only factor for the favorable property. The N_2 absorption-desorption isotherms and corresponding BJH pore-size distribution curves of S-600 and S-800 are displayed in Fig. S1.

3.5. Optical properties

The light absorption properties of the samples at different temperatures are presented in Fig. 6(a). It is shown that the light absorption properties of the samples have sharp change in the ultraviolet region (250–400 nm) and it decreases successively with increasing the roasting temperature, particularly for the lower absorptions on the samples

obtained at 600 °C, 700 °C and 800 °C in the formation of $\text{Zn}_2\text{V}_2\text{O}_7$ and ZnO. Instead, it is obvious that constructing ternary heterojunctions with $\text{Zn}_3(\text{VO}_4)_2$, the existence of $\text{Zn}_2\text{V}_2\text{O}_7$ and ZnO extends the range of spectrum response to visible light at 550 nm. Interestingly, it is found that the S-700 prepared by microwave hydrothermal method (the preparation of $\text{Zn}_3(\text{OH})_2\text{V}_2\text{O}_7 \cdot 2\text{H}_2\text{O}$ precursor) has a stronger absorption ability in the ultraviolet region, comparing with the S-700 prepared by precipitation assistant method, which maybe due to that the 3D hierarchical $\text{Zn}_3(\text{OH})_2\text{V}_2\text{O}_7 \cdot 2\text{H}_2\text{O}$ nanoplates obtained by the former can induce the strong interaction by constructing ternary heterojunctions and P-700 can be unable to do that.

The band gap energies for all as-prepared catalysts determined by the equation $(ah\nu)^2 = h\nu - E_g$ are shown in Fig. 6(b) and the obtained results are listed in Table 3, where α is the absorbance, $h\nu$ is the absorption energy, and E_g is the bandgap energy [42,43]. It presents that due to that the heterostructure build by phase transition, the calcinations can efficiently reduce the large band gap of $\text{Zn}_3(\text{OH})_2\text{V}_2\text{O}_7 \cdot 2\text{H}_2\text{O}$ semiconductor and promote the light absorption.

3.6. Surface properties and compositions

The infrared spectroscopy analysis was applied to clarify the surface properties of as-prepared samples. As shown in Fig. 7, it can be observed clearly that the broad absorption peaks of sample-U between 3111 and 3432 cm^{-1} are the characteristic stretch vibrations of the

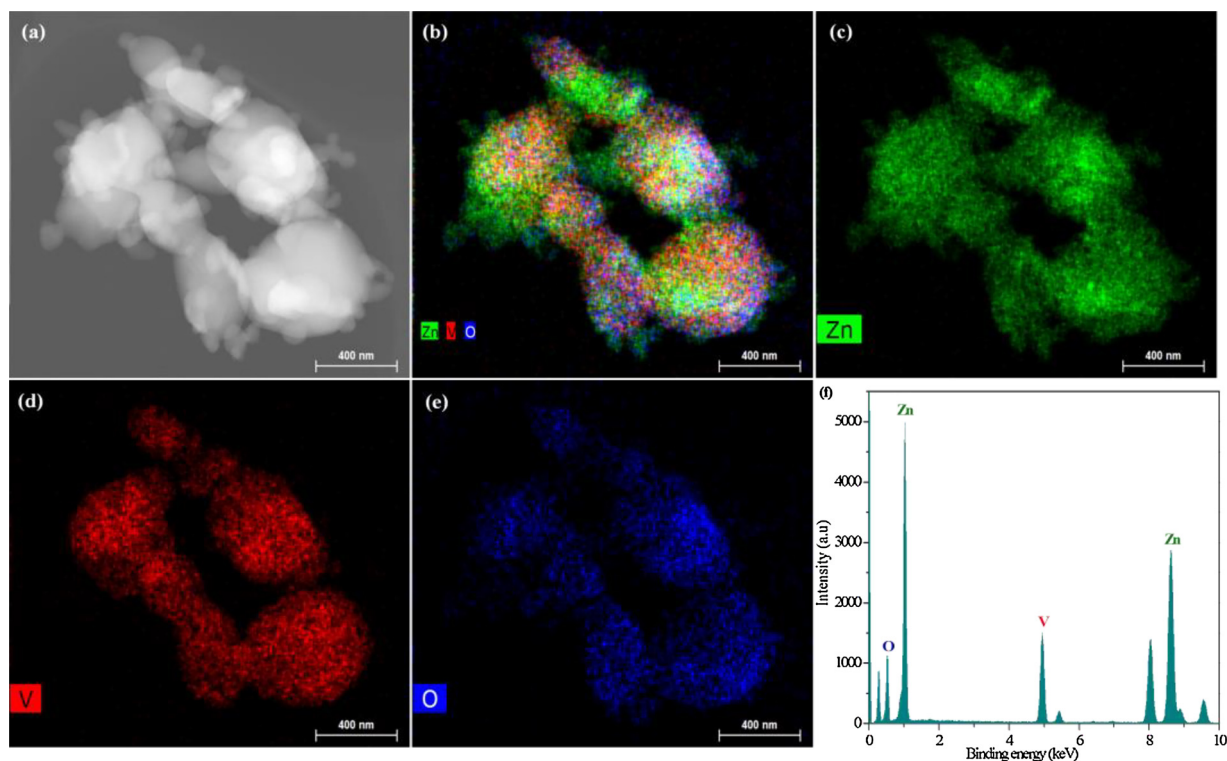


Fig. 4. TEM image and elemental mapping images of S-700. (a) TEM image; the element mapping of (b) all, (c) Zn, (d) V and (e) O.

surface hydroxyl groups and the absorption peak of 1634 cm^{-1} is provided by the adsorbed H_2O molecules [44,45]. The absorption peaks at 761 and 920 , 1400 cm^{-1} correspond to Zn-O and V-O bond vibrations, respectively [46,47]. The broad absorption peaks at $686\text{--}867\text{ cm}^{-1}$ present at S-400 and S-500, corresponding to asymmetric vibrations of V-O-Zn bond as well as intense stretching vibration of V-O-V bond originated from tetrahedral VO_4 [48]. For the phase transition at calcinating temperature of 600 and 700°C , the vibrational intensities at 661 , 790 , 840 and 901 cm^{-1} of V-O-Zn stretching vibration and tetrahedral VO_4 become obviously stronger and then that of sample calcined at 800°C starts to go down.

Raman spectrum was utilized to further confirm the composition and analyze the chemical interactions of all the samples. As Raman spectra of S-U shown in Fig. 8(a), the peaks at ~ 248 , ~ 323 , ~ 424 ,

Table 2

BET surface areas, pore volume, and pore size in the samples.

Sample	Surface Area (m^2/g) ^a	Pore Volume (cm^3/g) ^b	Pore Size (nm) ^c
S-U	17.40	0.079	27.64
S-500	20.59	0.087	21.91
S-600	8.13	0.023	11.75
S-700	5.26	0.011	8.91
S-800	0.11	0.001	—

^a BET surface area calculated from the linear part of the BET plot ($P/P_0 = 0.05\text{--}0.3$).

^b Total pore volume, taken from the volume of N_2 adsorbed at $P/P_0 = 0.995$.

^c Average pore diameter, estimated using the adsorption branch of the isotherm and the Barrett-Joyner-Halenda formula.

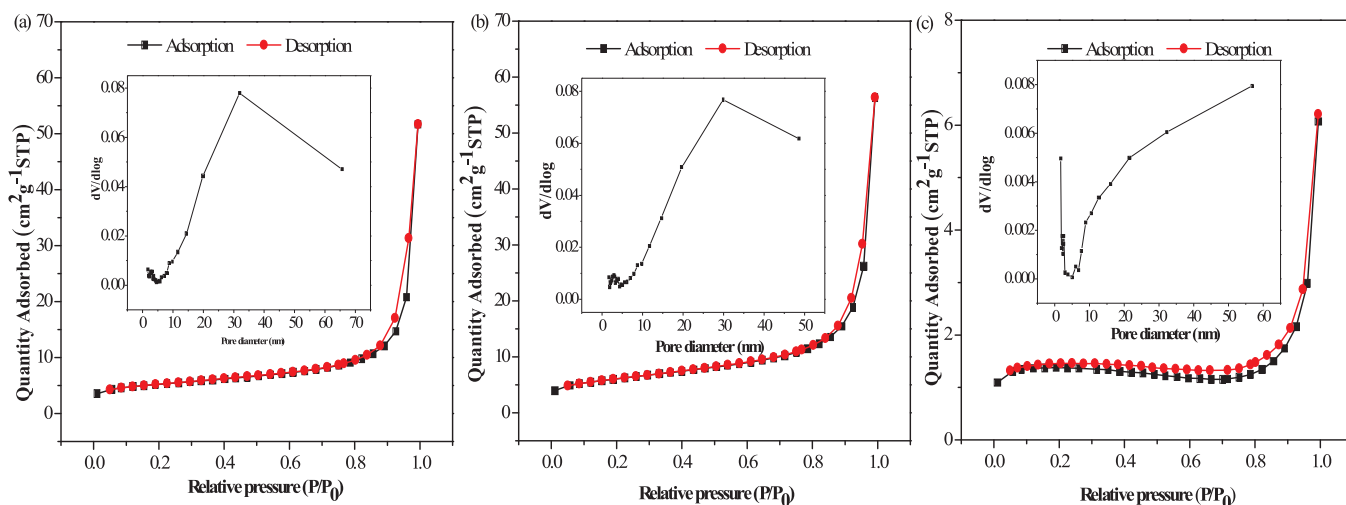


Fig. 5. The N_2 adsorption-desorption isotherms and corresponding BJH pore-size distribution curves (inset) for as-synthesized samples at different temperatures: (a) S-U ($\text{Zn}_3(\text{OH})_2\text{V}_2\text{O}_7 \cdot 2\text{H}_2\text{O}$); (b) S-500 and (c) S-700.

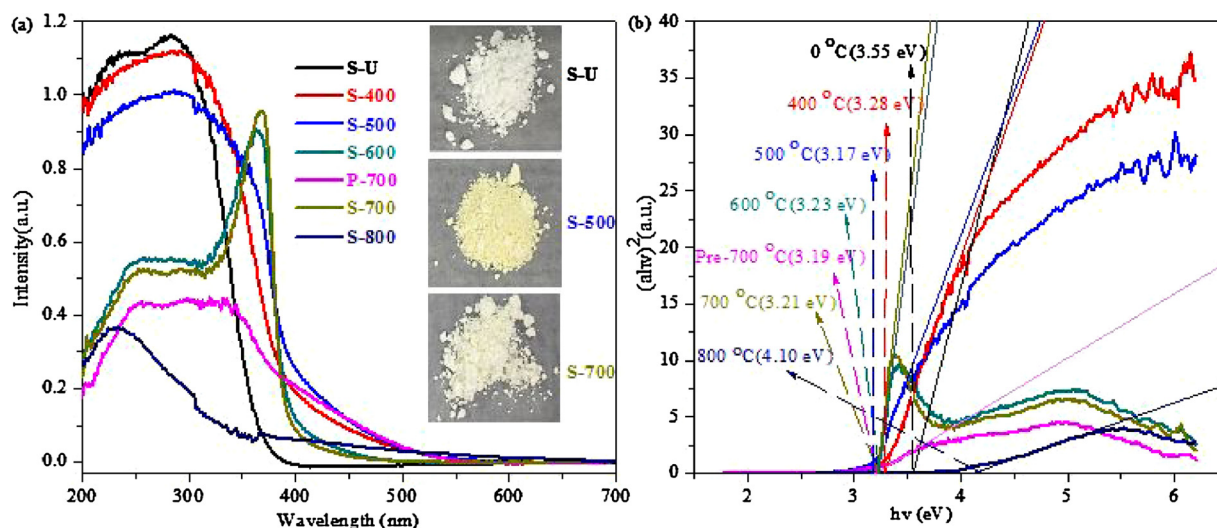


Fig. 6. (a) UV-vis absorption spectra of the prepared samples; (b) The curves of $(ah\nu)^2$ versus $h\nu$ for prepared samples.

Table 3

Band gap energies of the samples obtained at different temperatures.

Sample	Band energies (eV)	Sample	Band energies (eV)
S-U	3.55	S-400	3.28
S-500	3.10	S-600	3.23
S-700	3.18	S-800	4.10
P-700	2.67		

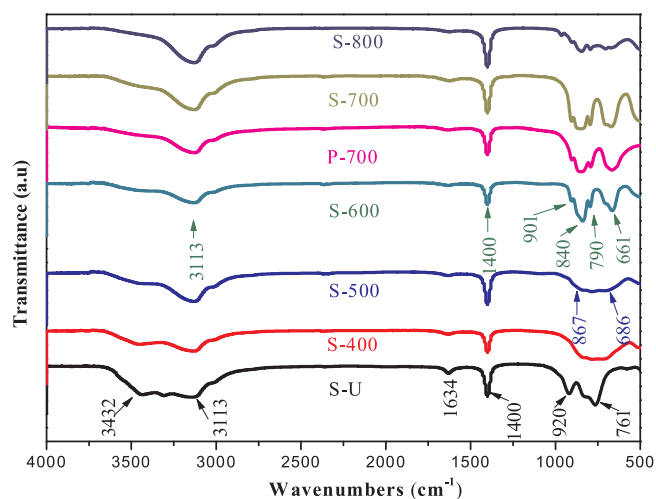


Fig. 7. IR spectra of the prepared samples.

~ 857 and $\sim 1356\text{ cm}^{-1}$ belong to $\text{Zn}_3(\text{OH})_2\text{V}_2\text{O}_7 \cdot 2\text{H}_2\text{O}$. Among them, peaks at ~ 248 and $\sim 323\text{ cm}^{-1}$ are attributed to the asymmetric stretching vibration of VO_4 . Peak at $\sim 424\text{ cm}^{-1}$ is assigned to the stretching bond of $\text{Zn}^{2+}-\text{O}^{2-}$ which can be observed in octahedral ZnO_6 and the vibrations at ~ 806 , 857 and 1356 cm^{-1} are attributed to $\text{V}^{5+}-\text{O}^{2-}$ stretching bond of tetrahedral VO_4 , respectively [49]. The surveys of S-400 and S-500 presented in Fig. 8(a) indicate that the vibrations of $\text{Zn}_3(\text{VO}_4)_2$ show up at ~ 168 , ~ 310 , ~ 811 (~ 823) and $\sim 1356\text{ cm}^{-1}$, where the peaks at ~ 811 (~ 823) and $\sim 1356\text{ cm}^{-1}$ are caused by the asymmetric stretching vibration of V–O bond corresponding to tetrahedral VO_4 [50] and $\sim 310\text{ cm}^{-1}$ are caused by the symmetry-related vibration and a weak peak at $\sim 168\text{ cm}^{-1}$ come from Zn–O vibration. For the formation of ternary heterojunction of $\text{Zn}_3(\text{VO}_4)_2/\text{Zn}_2\text{V}_2\text{O}_7/\text{ZnO}$ obtained at 600, 700 and 800 °C, it can be observed clearly in Fig. 8(b) that new peaks appear at ~ 266 , ~ 320 ,

~ 372 , ~ 396 , ~ 783 , ~ 850 , ~ 1454 and $\sim 1602\text{ cm}^{-1}$. Among them, ~ 850 and $\sim 1370\text{ cm}^{-1}$ come from symmetric stretching vibration of $\text{Zn}_3(\text{VO}_4)_2$, and wurtzite ZnO Raman modes exhibit at ~ 266 , ~ 372 and $\sim 396\text{ cm}^{-1}$ [51,52]. Furthermore, the others at ~ 783 , ~ 1454 as well as $\sim 1602\text{ cm}^{-1}$ are ascribed to the vibration of V–O bond in the tetrahedron VO_4 of $\text{Zn}_3(\text{VO}_4)_2$ and $\text{Zn}_2\text{V}_2\text{O}_7$ [53]. Importantly, the intensities of vibration peaks at ~ 168 , ~ 266 , ~ 320 , ~ 850 , ~ 1370 , ~ 1454 and $\sim 1602\text{ cm}^{-1}$ of S-600, S-700 and S-800 have an large enhancement comparing with S-U, S-400 and S-500. The intensities of the Raman peaks increase with the increasing of treatment temperature. Particularly, the strengthening peaks of Zn–O vibrations at ~ 168 , ~ 266 , ~ 372 and $\sim 396\text{ cm}^{-1}$ further confirm the construction of $\text{Zn}_3(\text{VO}_4)_2/\text{Zn}_2\text{V}_2\text{O}_7/\text{ZnO}$ and the progress of phase transition.

Meanwhile, the relationship between Raman stretching frequency and bond length is given by the following exponential form:

$$\nu = 21349 \times \exp(-1.9176 R_{\text{M-O}})$$

Here, ν is the Raman shift in wavenumbers and R is the metal–oxygen bond length in angstrom [54]. The lower Raman shift means the longer bond length. The calculations of the V–O bond lengths for the samples obtained by different roasting temperatures are presented in Table 4. It can be concluded that the V–O bond lengths of S-400 and S-500 increase by 0.027 and 0.020 Å, and then S-600, 700, 800 and P-700 exhibit a slower growth (greater than 0.004 Å) comparing with S-U, indicating that the local crystal structure of $\text{Zn}_3(\text{OH})_2\text{V}_2\text{O}_7 \cdot 2\text{H}_2\text{O}$ become loose with the increase of the calcinated condition. The moderate growth in bond length of Zn–O and V–O octahedrons is favorable for the generation, separation and transformation of photogenerated electron-hole pairs [55] produced by $\text{Zn}_3(\text{VO}_4)_2/\text{Zn}_2\text{V}_2\text{O}_7/\text{ZnO}$ heterojunction.

The surface chemical information of the typical S-700 sample was further checked by XPS measurement, including sample composition, purity and valence state. Fig. 9(a)–(d) shows the survey spectrum and the high-resolution XPS spectra for Zn 2p, V 2p and O 1s of S-700. As presented in Fig. 9(a), the existence of the carbon element is ascribed to the surface adventitious carbon from XPS itself. Apparently, high purity S-700 was successfully obtained. Fig. 9(b) indicates that two peaks with strong intensities of binding energies (BEs) at 1022.4 and 1045.5 eV correspond to Zn $2p_{3/2}$ and Zn $2p_{1/2}$, which is consistent with the report [56]. Fig. 9(c) shows that the Coster-Kronig Auger transition has occurred, where inner cores with a certain number electrons can be excited by high energy and released as Auger electrons, and then inner cores are rapidly filled by the equal number electrons from the high energy shell layers. Therefore, V $2p_{1/2}$ is wider than V $2p_{3/2}$ [57,58].

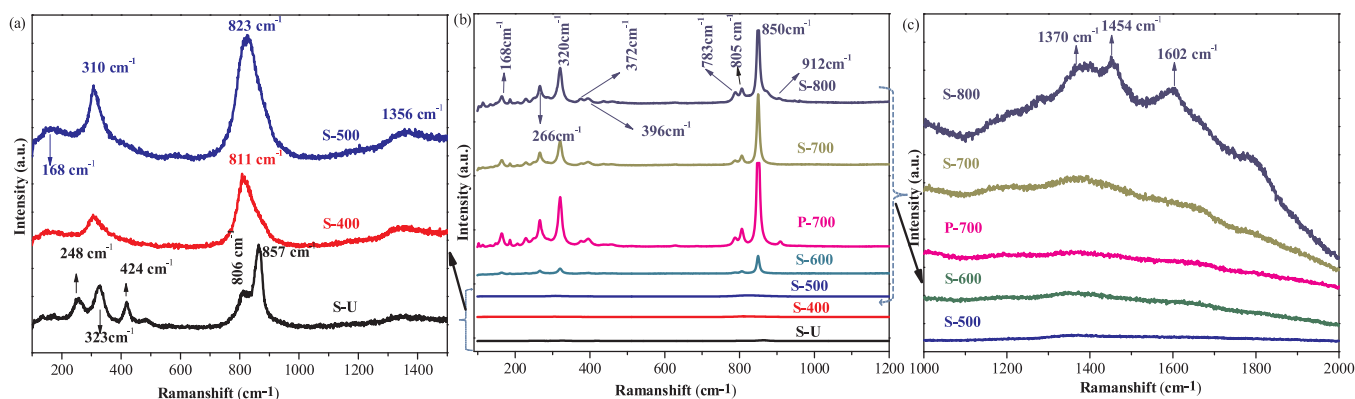


Fig. 8. Raman spectra of the prepared samples. (a) the enlarged figure of S-U, S-400 and S-500; (b) the figure of all the samples; (c) the figure from 1000 to 2000 cm^{-1} at the temperature of 500, 600, 700 and 800 $^{\circ}\text{C}$.

The BEs of V 2p at 516.6 and 524.1 eV are ascribed to $2p_{3/2}$ and $2p_{1/2}$, which are associated with the characteristic bands of oxidized V^{5+} in the crystalline $\text{Zn}_3(\text{VO}_4)_2$ or $\text{Zn}_2\text{V}_2\text{O}_7$. Fig. 9(c) suggests that the peak located at 529.9 eV in the O 1s spectrum can be assigned to lattice O^{2-} ions of S-700 bound with Zn or V in crystalline $\text{Zn}_3(\text{VO}_4)_2$ and $\text{Zn}_2\text{V}_2\text{O}_7$ lattice, the other two peaks located at the near 531.0 eV and 532.3 eV that associated with the hydroxide or hydroxyl groups on the surface of the sample [59,60].

3.7. PL properties

Photoluminescence (PL) spectra is an effective mean for revealing the fate of photogenerated charge carriers [61]. It is well known that the lower emission intensity of PL implies the better separation efficiency of photogenerated electron-hole pairs [14,62]. Fig. 10 exhibits the PL spectra of as-prepared samples with the emission wavelength of 350 nm for two main reasons: the quantum size effect and structural defects in the crystals. It has been well known that zinc vacancy, oxygen vacancy, interstitial oxygen or zinc may induce new energy levels in the band gap [63] and PL of the sample can be inhibited when the sample size gets smaller. Depending on the particle size and exciting wavelength, S-U, S-400 and S-500 show the weak emission peaks centered at around 466 nm, which maybe the low atom vacancies and the small sizes of well-dispersed nanosheets from SEM analysis. Interestingly, the emission intensities at S-600, P-700, S-700 and S-800 are much stronger than that of the lower temperature and the visible light emission peaks appear at around 538 nm, corresponding to the green emission. This maybe due to that the heterojunction by the phase transition at high temperature possesses the atom vacancies, improving the photo-response of the photocatalyst and producing more photogenerated e^-/h^+ pairs. For S-600, S-700 and S-800, the separation efficiencies of e^-/h^+ pairs enhance with the raising of the calcined temperature. Moreover, the P-700 sample obtained by microwave assisting method exhibits a lower intensity of PL emission than that prepared by precipitation assistant, which should be attributed to better crystallinity of S-700 by microwave method in favor of the separation of photoinduced carriers from XRD analysis.

Table 4

The bond lengths of V–O of the synthesized samples.

Sample	Raman shift (cm^{-1})	Bond lengths of V–O (\AA)	Sample	Raman shift (cm^{-1})	Bond lengths of V–O (\AA)
S-U	V–O:857	V–O:1.759	S-400	V–O:811	V–O:1.786(+0.027 ^a)
S-500	V–O: 823	V–O:1.779(+0.020 ^a)	S-600 (700, 800, P-700)	V–O:850	V–O:1.763(+0.004 ^a)

^a The increased bond lengths of V–O comparing with S-U sample, estimated by the formula on the basis of the relationship of Raman stretching frequency and bond length.

3.8. Photocatalytic performances

The photocatalytic performances of the synthesized samples fabricated at different temperatures were evaluated by the photodegradation of the typical simulation pollutants, such as phenols (e.g., phenol, P-chlorophenol and bisphenol A). Fig. 11(a) shows that S-600, S-700 and S-800 exhibit good performance on the photocatalytic activities for phenols degradation, in which $\text{Zn}_3(\text{VO}_4)_2/\text{Zn}_2\text{V}_2\text{O}_7/\text{ZnO}$ ternary heterojunction is helpful to largely enhance the photocatalytic performance. Particularly, S-700 exhibits the highest photocatalytic activity for phenols decomposition, which is greatly suitable for the application of the degradation of phenols because of the achievement of 98% in the degradation rate over the P-chlorophenol comparing with the degradation rate of 77% over the biphenol A and 75% over the phenol within the 150 min. Although the surface area of S-700 is lower than that of S-U and S-500, it performs most efficient, indicating that the adsorption and activation of the reactants on the micropores could not be the rate-determining step in the photocatalytic degradation process. The total organic carbon (TOC) removal rates of phenols and the degradation rate of dyes over different samples are presented in Fig. S2. Table S1 summarized the TOC removal rates of phenols. We can see that S-700 sample gives the highest TOC removal rates. The TOC remove rates for phenol, P-chlorophenol, and bisphenol over S-700 are 72.0%, 91.2% and 75.5%, respectively.

To confirm whether the remarkable enhanced photoactivity is general, these above samples were chosen to further evaluate the photocatalytic activity for the degradation of organic dyes (e.g., Rh B, MO, Acid orange II and MB), as presented in Fig. 11(b). It can be concluded clearly that given its favorable structure for the formation of $\text{Zn}_3(\text{VO}_4)_2/\text{Zn}_2\text{V}_2\text{O}_7/\text{ZnO}$ ternary heterojunction, S-700 performs the best photocatalytic degradation, achieving a maximum degradation rate of 88.99, 56.86 and 83.29% for Rh B, MO and Orange II within 75 min and 89.55% for MB in 30 min except the presence of self-decomposition under the light irradiation. And the sequence of photocatalytic performances is as follows: S-700 > S-600 > S-800 > P-700 > S-500 > S-400. By comparison, as the single component photocatalyst of $\text{Zn}_3(\text{VO}_4)_2$, the photocatalytic performances of S-400 and S-500 show a lower tendency, suggesting that the synergistic interaction among $\text{Zn}_3(\text{VO}_4)_2$, $\text{Zn}_2\text{V}_2\text{O}_7$ and ZnO is required to optimally

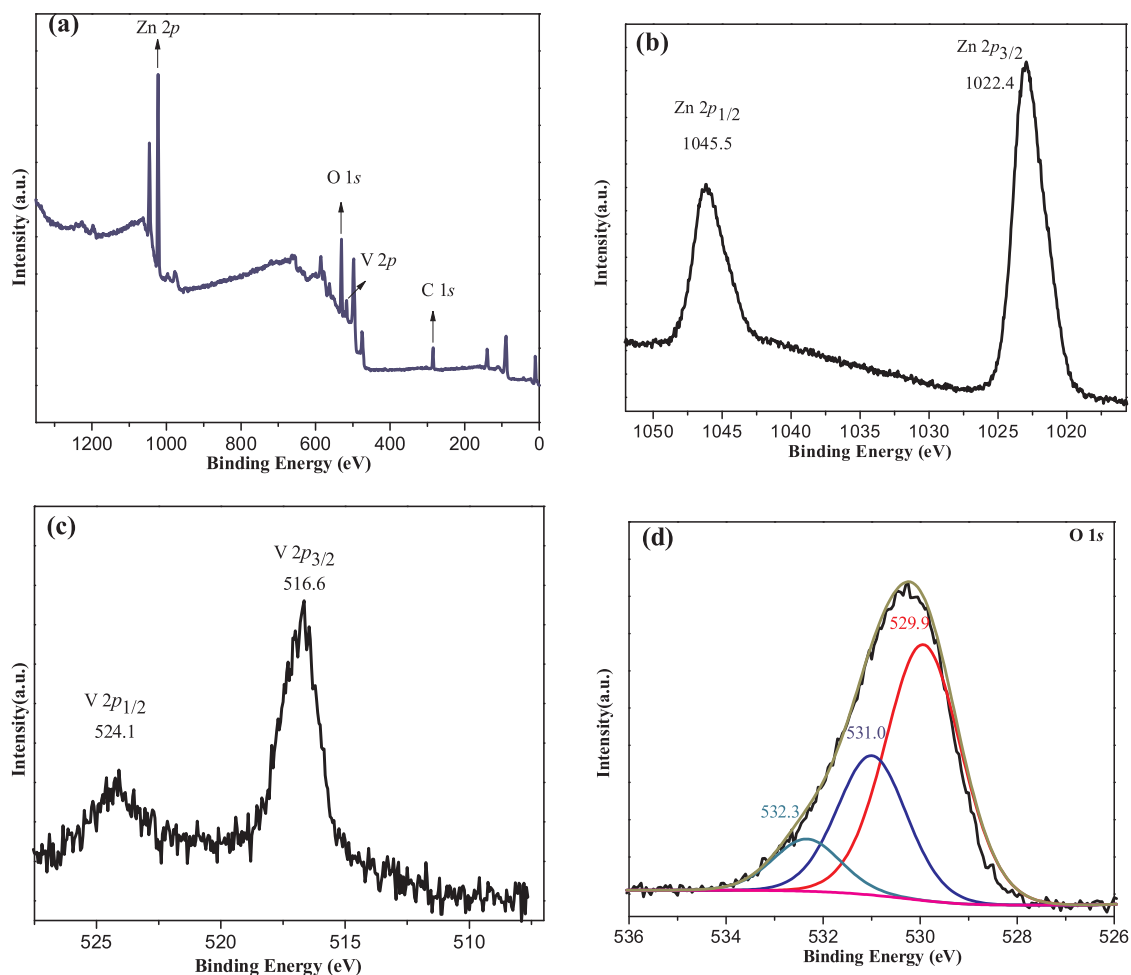


Fig. 9. XPS spectra of the typical S-700 sample. (a) Survey spectrum; High-resolution spectrum: (b) Zn 2p; (c) V 2p; (d) O 1s.

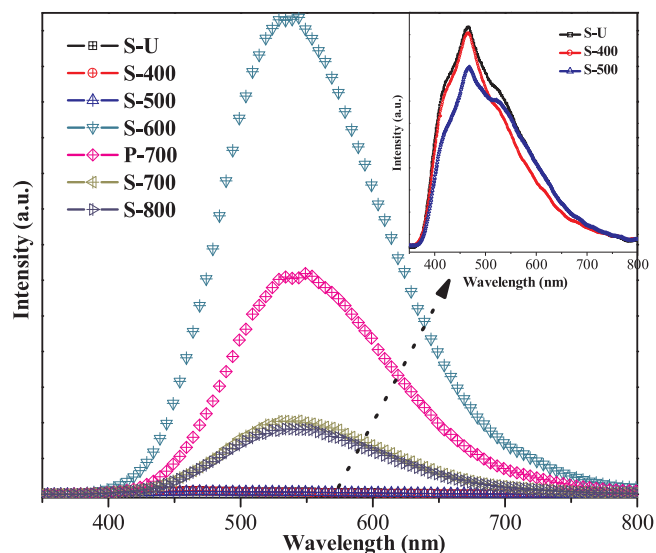


Fig. 10. Photoluminescence (PL) spectra of the fabricated samples.

enhance the photoactivity of semiconductor $\text{Zn}_3(\text{VO}_4)_2$. For instance, the photoactivity of S-800 is lowered greatly as compared to that of optimized ternary heterojunctions. On one hand, the change of the relative weight ratio on the surface maybe shield the light from being absorbed by $\text{Zn}_3(\text{VO}_4)_2$ with a wide light response as seen from DRS, which is called a light “shielding effect” [64]. It has been reported that

zinc pyrovanadate has an interesting hexagonal crystal structure of alternated Zn–O layer and V–O layer with channels in V–O layer, which will facilitate the migration of carriers to the surface of the catalyst [65]. On the other hand, the higher calcinating temperature leads to the blocking of the active sites on the photocatalyst surface and also reduces the efficiency of light passing through the depth of the medium. As we all know [66], if the samples hold a same shape, smaller-scale sample with a porous structure by facilitating the molecular transport of reactants and products may have higher utilization of carriers or sunlight and a higher photocatalytic activity. Therefore, the high photocatalytic activity of ternary heterojunction nanosheets could be ascribed to the synergistic consequence of hierarchical architecture, better light response, special heterojunction structure, and high utilization of carriers.

Moreover, to test the stability of the best composite photocatalyst (S-700), the recycle test in degradation of Rh B was carried out as shown in Fig. 11(c). An overall view of the photoactivity steers us to the finding that the activity of the hybrid photocatalyst only shows a slight change with a good performance for Rh B degradation and the degradation rate of 80.41% in 75 min after five successive cycles was maintained, which indicates that $\text{Zn}_3(\text{VO}_4)_2/\text{Zn}_2\text{V}_2\text{O}_7/\text{ZnO}$ ternary photocatalyst has good stability and promising applications in environmental remediation. The supplemental information of XRD patterns {Fig. S3(a)}, FT-IR {Fig. S3(b)} and SEM {Fig. S3(c)} of S-700 and S-700 after 5th run cycle photocatalytic experiments confirm that there are no evident change in crystalline structure, vibrational intensities and morphology structures, which further confirmed the chemical stability of Z-scheme $\text{Zn}_3(\text{VO}_4)_2/\text{Zn}_2\text{V}_2\text{O}_7/\text{ZnO}$ ternary heterojunction.

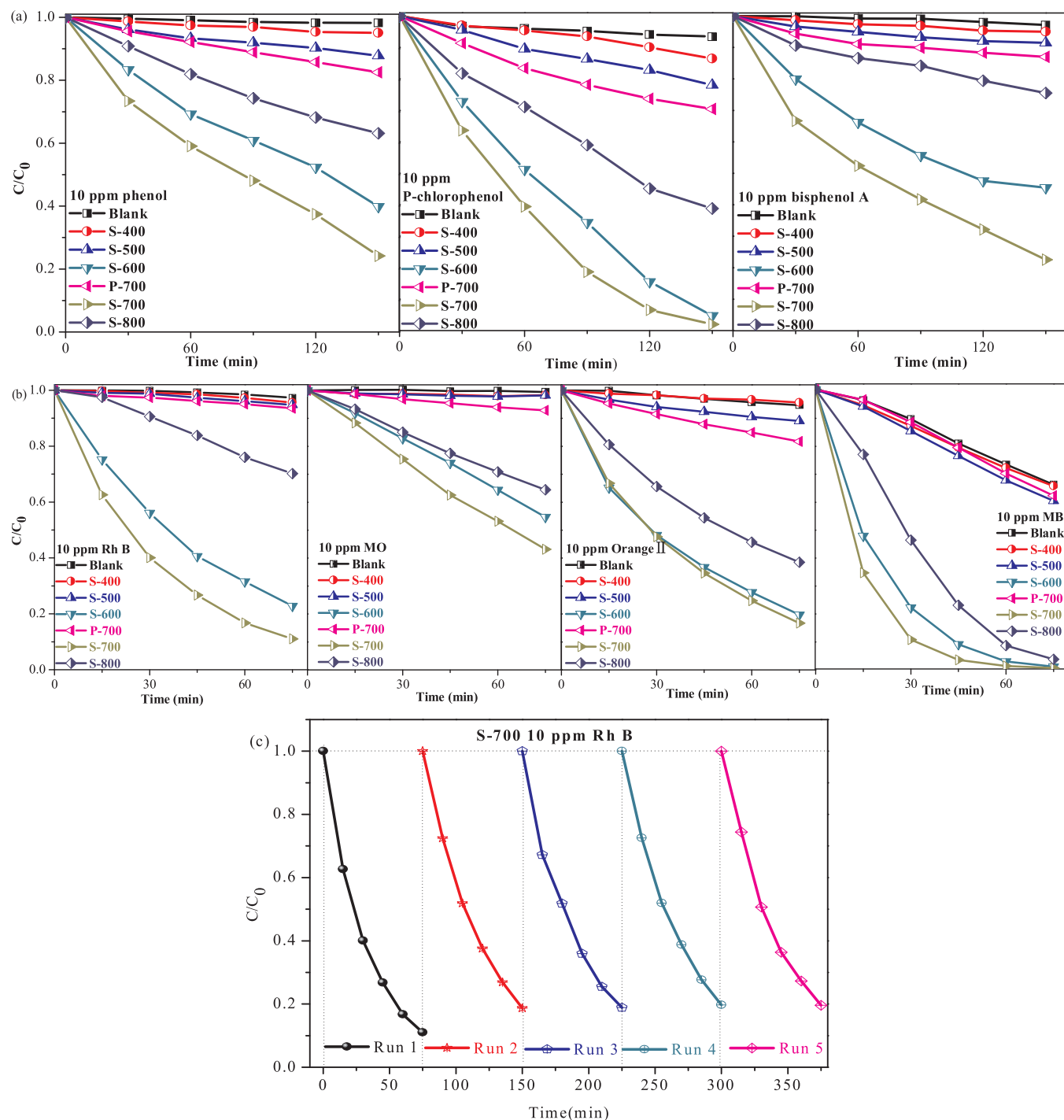


Fig. 11. Comparison of photocatalytic performances of as-prepared samples: (a) phenols (phenol, P-chlorophenol and bisphenol); (b) dyes (Rh B, MO, Orange II and MB); (c) Photocatalytic stability of S-700 in recycling reactions for the degradation of Rh B.

3.9. Discussion

$\text{Zn}_3(\text{VO}_4)_2/\text{Zn}_2\text{V}_2\text{O}_7/\text{ZnO}$ ternary hybrids did perform the enhanced photocatalytic performances for the higher migration, transfer and separation efficiency of photogenerated electron-hole pairs as the key parameters during the photocatalytic process. To understand the mechanism for enhanced activity, we have performed some other characterizations, including electrochemical analysis, ESR and trapping experiments of reactive active species. To evaluate the photoconversion efficiency and charge transfer property, photoelectrochemical experiments were applied to reveal the dynamic characteristics of

photogenerated charges over semiconductor photocatalysts, in which a stronger photocurrent and a lower impedance indicate more excellent light response capability and higher separation efficiency of photo-generated e^-/h^+ pairs [67]. As indicated by Fig. 12(a) for photo-electronic transformation of the series of samples obtained under different conditions, all samples, more or less, have a photocurrent response for each light-on event and the transient photocurrent intensity of the S-700 sample is the strongest and stable (photocurrent value of $\sim 0.729 \mu\text{A}$), which is about 91 times as high as that of S-U ($\text{Zn}_3(\text{OH})_2\text{V}_2\text{O}_7 \cdot 2\text{H}_2\text{O}$) and equal to 34 times higher than that of S-500 ($\text{Zn}_3(\text{VO}_4)_2$). It indicates that $\text{Zn}_3(\text{VO}_4)_2/\text{Zn}_2\text{V}_2\text{O}_7/\text{ZnO}$ heterostructure

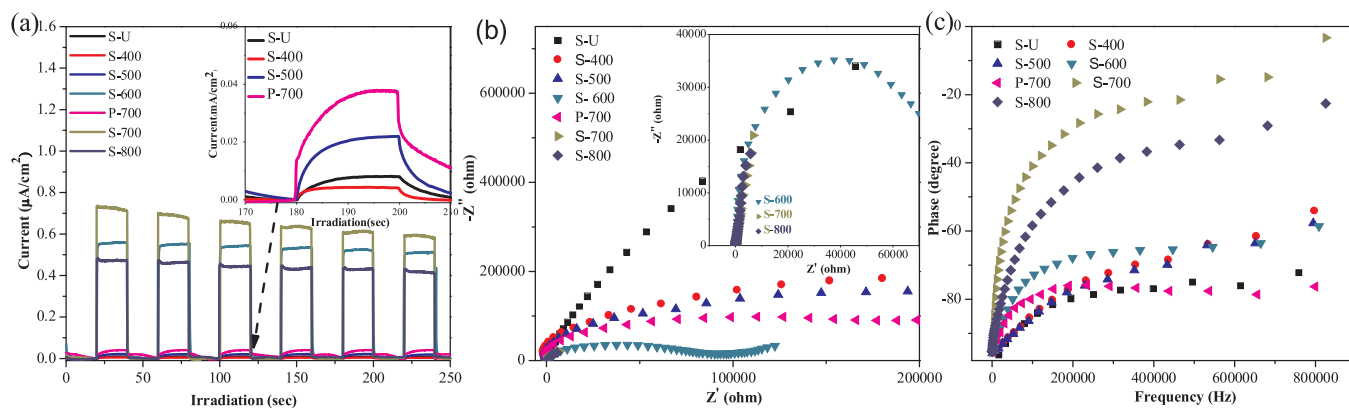


Fig. 12. Photoelectrochemical measurements of samples. (a) Comparison of transient photocurrent response of synthesized samples; (b) EIS Nyquist plots of the prepared samples; (c) Bode-phase of the obtained samples.

can produce more photogenerated electron-hole pairs and hold an improved separation efficiency. Instead, S-U, S-400 and S-500 samples with weaker light response capability (lower photocurrent) generate only the small amounts of photogenerated electron-hole pairs, corresponding to lower recombination rate of photogenerated carriers, almost consistent with the PL result. Moreover, the photocurrent intensity of S-500 is stronger than that of S-400 due to the improvement of crystallinity and the intensity of S-800 is lower than that of S-700 because of the change of surface states.

Similarly, electrochemical impedance spectroscopy (EIS) was used to expound the transfer and migration processes of photo-generated electron-hole pairs, and the results are shown in Fig. 12(b), the typical smaller EIS arc radius reflects the lower charge transfer resistance of the double-layer capacitance in parallel at the interfacial layer between the working electrode and electrolyte solution, representing higher charge transfer efficiency [68]. S-600, S-700 and S-800 electrodes among those electrodes exhibit the most depressed semicircle at high frequency, suggesting that the smaller resistance and more efficient transfer of charge carriers between electrode and electrolyte solution are obtained over $\text{Zn}_3(\text{VO}_4)_2/\text{Zn}_2\text{V}_2\text{O}_7/\text{ZnO}$ heterostructure than those over S-U, P-700 and $\text{Zn}_3(\text{VO}_4)_2$ electrodes. The enhanced transfer and the repressed recombination of photogenerated charge carriers are contributive to the high photoactivity as observed above.

In addition, from the Bode-phase spectra as indicated in Fig. 12(c), with the increase of temperature, the characteristic mid-frequency peak of the electrode which is located at the peak frequency (f_{\max}) of the intermediate frequency semicircle gradually shifts to a lower frequency, corresponding to an increase of the electron lifetime (τ) and a faster electron transport process. According to the relation $\tau = 1/(2\pi f_{\max})$ and the characteristic frequency f_{\max} of the electrode at the top of the low frequency arc [69], the electronic lifetime (τ) can be derived as shown in Table 5. Among them, the characteristic frequency of the S-700 is shifted to the lowest value compared with the high frequency of 325,928.6 Hz over S-U, revealing its longevity of electrons (1.38 μs) and the fastest electron transfer. As indicated by the data, the electron lifetime of S-700 is 1.82 times (0.49 μs) and 1.20 times (0.63 μs) longer than that of $\text{Zn}_3(\text{OH})_2\text{V}_2\text{O}_7 \cdot 2\text{H}_2\text{O}$ and $\text{Zn}_3(\text{VO}_4)_2$, respectively. The electron lifetime improvement indicates that $\text{Zn}_3(\text{VO}_4)_2/\text{Zn}_2\text{V}_2\text{O}_7/\text{ZnO}$

heterostructure greatly represses the recombination of photogenerated e^-/h^+ pairs and promote the migration process.

To understand the role of photogenerated active species and explore the underlying photocatalytic mechanism for the enhanced photocatalytic performance, the blank or trapped experiments with the addition of various radical scavengers on S-700 were carried out to evaluate the photocatalytic performance of Rh B (Fig. 13(a)). Trapped experiments taking tert-butyl alcohol (TBA, 1 mM), p-benzoquinone (p-BZQ, 1 mM) and disodium ethylenediaminetetraacetate ($\text{Na}_2\text{-EDTA}$, 1 mM) as the radical scavenger of hydroxyl radicals ($\cdot\text{OH}$), superoxide radicals ($\cdot\text{O}_2^-$) and photogenerated holes, respectively, clearly suggest that, the addition of p-BZQ and $\text{Na}_2\text{-EDTA}$ extremely weaken the photocatalytic performance of S-700 for the degradation rate of RhB from 88.98% to 11.87% (p-BZQ) and 24.15% ($\text{Na}_2\text{-EDTA}$) in 75 min. And while, the addition of TBA reduces the degradation rate of RhB to 55.37%, demonstrating that the primary active radical species are photogenerated holes, electrons and activated oxygen (e.g., $\cdot\text{OH}$ and $\cdot\text{O}_2^-$, which presences are further confirmed by the ESR spectra analysis in Fig. 13(b) and (c) under UV light irradiation).

During ESR testing, the lifetimes of $\cdot\text{OH}$ and $\cdot\text{O}_2^-$ were so short that DMPO (5, 5-dimethyl-1-pyrroline N-oxide) was taken as trapping agent in H_2O and methanol dispersion, respectively [70,71]. Fig. 13b and c shows that no ESR signals are detected when S-500 and S-700 were performed in the dark condition, confirming that the reaction is really actuated by a photocatalytic process. According to the traditional transfer mechanism of photoinduced electron-hole pairs, the redox ability would be reduced for the electrons and holes after transferring to lower CB or VB, which could cause a decline of ESR signals of $\text{DMPO} \cdot \cdot\text{OH}$ and $\text{DMPO} \cdot \cdot\text{O}_2^-$ [25]. Despite the fact that the CB of $\text{Zn}_3(\text{VO}_4)_2$ is positive than standard redox potential $E_0(\text{O}_2/\cdot\text{O}_2^-)$, we still observe a strong ESR signal of $\cdot\text{O}_2^-$, which could be due to the donor defect sites of semiconductor that favor enriching of electron in the conduction band [72].

However, although the ESR signals of $\text{DMPO} \cdot \cdot\text{OH}$ have enhanced greatly, the $\text{DMPO} \cdot \cdot\text{O}_2^-$ of the typical S-500 ($\text{Zn}_3(\text{VO}_4)_2$) and S-700 ($\text{Zn}_3(\text{VO}_4)_2/\text{Zn}_2\text{V}_2\text{O}_7/\text{ZnO}$) samples was enhanced slightly, revealing that the photoinduced electrons in the CB of $\text{Zn}_2\text{V}_2\text{O}_7$ and ZnO tend to transfer and recombine with the photoinduced holes in the VB of $\text{Zn}_3(\text{VO}_4)_2$ [27]. Moreover, photoinduced holes accumulated in VB of $\text{Zn}_2\text{V}_2\text{O}_7$ and ZnO would directly break down the organic pollutants into small molecules or oxidate the $-\text{OH}$ group to produce $\cdot\text{OH}$, which is in good line with the enhanced photocatalytic performance. Thus, we could infer that the photocatalytic reaction in this $\text{Zn}_3(\text{VO}_4)_2/\text{Zn}_2\text{V}_2\text{O}_7/\text{ZnO}$ ternary heterojunction follows a double Z-scheme mechanism, which greatly improve the separation and transfer of photoinduced electron-hole pairs as well as enhance the strong oxidation ability for organic pollutants degradation [26]. Combining the control experiments of reactive active species with ESR test, we can summarize that

Table 5
The electronic lifetimes (τ) of the synthesized samples.

Samples	f_{\max} [Hz]	τ [μs]	Samples	f_{\max} [Hz]	τ [μs]
S-U	325,928.6	0.49	S-400	282,738.1	0.56
S-500	252,952.4	0.63	S-600	160,809.5	0.99
S-700	115,571.4	1.38	S-800	176,642.8	0.90
P-700	189,761.9	0.84			

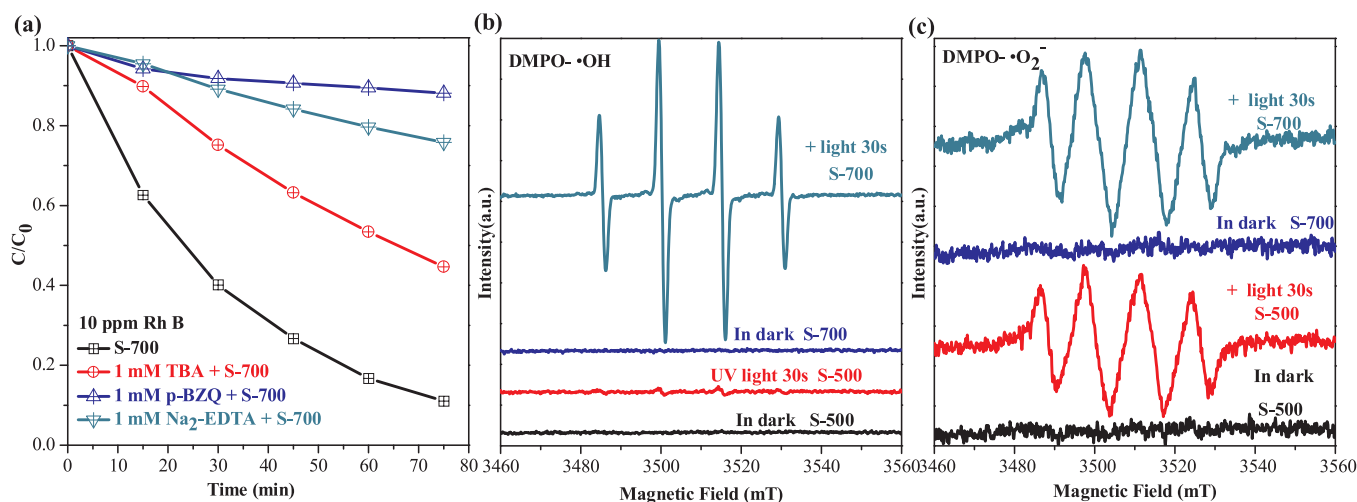


Fig. 13. The detection of the main active species: (a) The effects of the addition of tert-butyl alcohol (TBA), benzoquinone (p-BZQ) and disodium ethylenediaminetetraacetate (Na₂-EDTA) on the degradation rate of RhB over S-700; (b) ESR signals of DMPO·OH and (c) DMPO·O₂⁻ over the typical S-500 and S-700 samples.

although ·OH is an active oxygen species involved in the photocatalytic reactions, h^+ and ·O₂⁻ play more important role on the efficient removal of Rh B.

The reason of the enhanced photocatalytic performance as well as the relationship between the conduction band (CB) and valence band (VB) of the ternary catalytic system can be revealed by the charge transfer between the band positions of Zn₃(VO₄)₂, Zn₂V₂O₇ and ZnO. The values of CB and VB were calculated by the following formula:

$$E_{CB} = X - E_e - 0.5E_g$$

$$E_{VB} = E_{CB} + E_g$$

where E_{VB} and E_{CB} represent edge potentials of the valence band and the conduction band, respectively. And X is the absolute electronegativity of the semiconductor, E_e is the energy of free electrons on the hydrogen scale (the value of E_e is generally 4.5 eV), and E_g is the band gap energy of the semiconductor [73]. It is reported that the band gap energy of Zn₃(VO₄)₂ is 2.44 eV [74], and while the band gap energies over Zn₂V₂O₇ [75] and ZnO [76] are 3.23 eV and 3.20 eV, respectively. The calculated result of Zn₃(VO₄)₂, Zn₂V₂O₇ and ZnO about X values, E_{VB} and E_{CB} edge potentials versus normal hydrogen electrode (NHE) are shown in Table 6.

On the basis of the above discussion, it can be concluded that the enhanced photocatalytic performance of the ternary Zn₃(VO₄)₂/Zn₂V₂O₇/ZnO hybrids can be attributed to the better light absorption capacity, the longer lifetime of photogenerated e^-/h^+ pairs, and faster interfacial charge transfer. As well known [77], Fermi level (E_F) equals to the Mott-Schottky relationship for n-type semiconductor and the changes of electronic state on the samples was analyzed by the Mott-Schottky plots as indicated by Fig. 14. Obviously, Fermi level (E_F) of S-700 and S-800 ternary hybrids shifts negatively in comparison with that of Zn₃(VO₄)₂ (S-500) from the Fermi-level equilibration in accordance with the calculated CB edges of Zn₃(VO₄)₂, Zn₂V₂O₇ and ZnO in Table 6. Under the ultraviolet irradiation, the electrons are excited from their VB to its CB, which transfer to Zn₂V₂O₇ and then to Zn₃(VO₄)₂

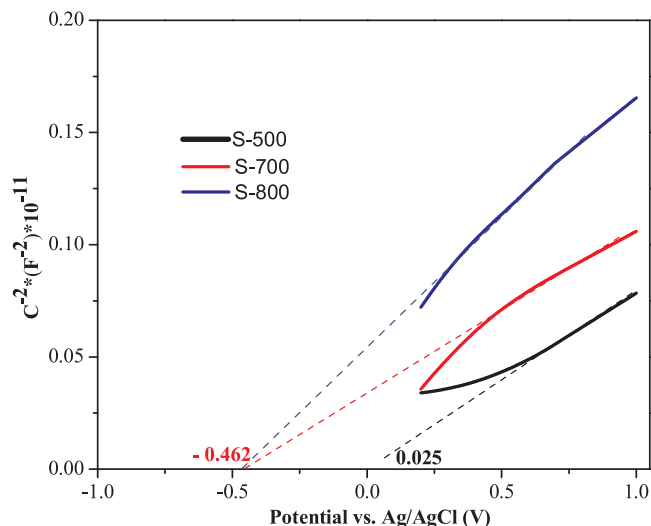


Fig. 14. Mott-Schottky (MS) plots for the S-500, S-700 and S-800 samples.

owing to themselves intimate interfacial contact. The accumulated electrons inevitably induces shifting of the apparent E_F to achieve equilibrium and they react with the adsorbed or dissolved oxygen molecules to give superoxide radicals. Also, according to the values of energy band, this transfer process of photogenerated holes from Zn₂V₂O₇ to Zn₃(VO₄)₂ and ZnO is thermodynamically permissible, thereby producing the high performance. Moreover, the characterization results of XRD and thermal analysis make clear that as the increase of calcinated temperature Zn₃(OH)₂(VO₄)₂·2H₂O lost its H₂O to generate Zn₃(VO₄)₂ and then the partial Zn₃(VO₄)₂ undergo phase transition to produce Zn₂V₂O₇ and ZnO. UV-vis absorption, PL spectra, photoelectrochemical and ESR experiments indicate that ternary heterojunction constructed by phase transition improves the transfer of photogenerated electron-hole pairs, widens the photoresponse and produces more active oxidizing species for photocatalytic reaction purifying target pollutants, such as h^+ , ·OH and ·O₂⁻. Accordingly, a probable double Z-scheme reaction mechanism of S-700 has been proposed, as illustrated in Scheme 1.

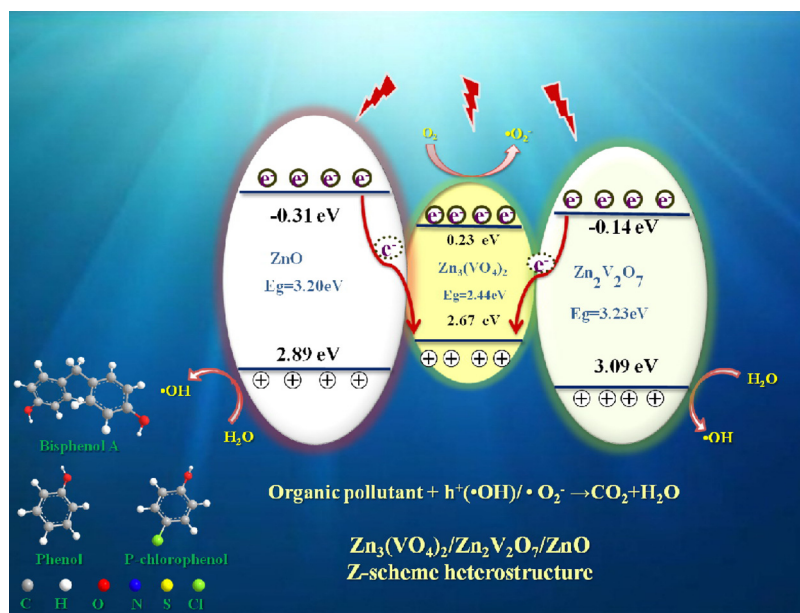
4. Conclusions

In summary, a novel, efficient and stable double Z-scheme Zn₃(VO₄)₂/Zn₂V₂O₇/ZnO ternary heterojunction has been facilely and

Table 6

The calculated results of Zn₃(VO₄)₂, Zn₂V₂O₇ and ZnO about X values, E_{VB} and E_{CB} .

Samples	X value (eV)	E_{VB} (eV)	E_{CB} (eV)
Zn ₃ (VO ₄) ₂	5.95	2.67	0.23
Zn ₂ V ₂ O ₇	5.98	3.09	-0.14
ZnO	5.79	2.89	-0.31



Scheme 1. The possible photocatalytic process of organic pollutants over $\text{Zn}_3(\text{VO}_4)_2/\text{Zn}_2\text{V}_2\text{O}_7/\text{ZnO}$ system.

low-costly synthesized by a microwave hydrothermal assistant and one-step calcining process. The phase transformation process of $\text{Zn}_3(\text{OH})_2\text{V}_2\text{O}_7 \cdot 2\text{H}_2\text{O}$ can be defined that the dehydration of $\text{Zn}_3(\text{OH})_2\text{V}_2\text{O}_7 \cdot 2\text{H}_2\text{O}$ was to form $\text{Zn}_3(\text{VO}_4)_2$ and then the partial $\text{Zn}_3(\text{VO}_4)_2$ undergo phase transition to produce $\text{Zn}_2\text{V}_2\text{O}_7$ and ZnO ($\text{Zn}_3(\text{OH})_2\text{V}_2\text{O}_7 \cdot 2\text{H}_2\text{O} \rightarrow \text{Zn}_3(\text{VO}_4)_2 \rightarrow \text{Zn}_2\text{V}_2\text{O}_7 + \text{ZnO}$). The results show that the double Z-scheme ternary hybrid exhibit much higher visible light photoactivity than $\text{Zn}_3(\text{VO}_4)_2$ toward the degradation of the simulation pollutants, which can be ascribed to the combined interaction of the longer lifetime of photogenerated e^- , faster interfacial charge-transfer and wider light-response. This work highlights the importance of design the double Z-scheme in semiconductor heterostructure system with high photocatalytic performance over the vanadate via phase transformation process. The spotlight of discovery in this work could provide new theory and road into create and utilize multicomponent photocatalysts.

Acknowledgements

The support from the National Natural Science Foundation of China (21567008, 21263005, 21607064, 21707055), Program of Qingjiang Excellent Young Talents, Jiangxi University of Science and Technology, Program of 5511 Talents in Scientific and Technological Innovation of Jiangxi Province (20165BCB18014), Academic and Technical Leaders of the Main Disciplines in Jiangxi Province (20172BCB22018), Jiangxi Province Natural Science Foundation (20161BAB203090), the Young Science Foundation of Jiangxi Province Education Office (GJJ160671), and the Open Project Program of the State Key Laboratory of Photocatalysis on Energy and Environment (SKLPEE-KF201712) in Fuzhou University is gratefully acknowledged.

Appendix A. Supplementary data

Supplementary material related to this article can be found, in the online version, at doi:<https://doi.org/10.1016/j.apcatb.2018.06.010>.

References

- [1] M.A. Shannon, P.W. Bohn, M. Elimelech, J.G. Georgiadis, B.J. Marinas, A.M. Mayes, Science and technology for water purification in the coming decades, *Nature* 452 (2008) 301–310.
- [2] X. Sheng, Z. Liu, R. Zeng, L.P. Chen, X.J. Feng, L. Jiang, Enhanced photocatalytic reaction at air–liquid–solid joint interfaces, *J. Am. Chem. Soc.* 139 (2017) 12402–12405.
- [3] M.R. Hoffmann, S.T. Martin, W.Y. Choi, D.W. Bahnemann, Environmental applications of semiconductor photocatalysis, *Chem. Rev.* 95 (1995) 69–96.
- [4] F. Chen, Q. Yang, Y. Zhong, H.X. An, J.W. Zhao, T. Xie, Q.X. Xu, X.M. Li, D.B. Wang, G.M. Zeng, Photo-reduction of bromate in drinking water by metallic Ag and reduced graphene oxide (RGO) jointly modified BiVO_4 under visible light irradiation, *Water Res.* 101 (2016) 555–563.
- [5] S.F. Yang, C.G. Niu, D.W. Huang, H. Zhang, C. Liang, G.M. Zeng, SrTiO_3 nanocubes decorated with Ag/AgCl nanoparticles as photocatalysts with enhanced visible-light photocatalytic activity towards the degradation of dyes, phenol and bisphenol A, *Environ. Sci. Nano* 4 (2017) 585–595.
- [6] J. Tian, Z. Wu, Z. Liu, C.L. Yu, K. Yang, L.H. Zhu, W.Y. Huang, Y. Zhou, Low-cost and efficient visible-light-driven $\text{CaMg}(\text{CO}_3)_2/\text{Ag}_2\text{CO}_3$ microspheres fabricated via an ion exchange route, *Chin. J. Catal.* 38 (2017) 1899–1908.
- [7] R.B. Wei, Z.L. Huang, G.H. Gu, Z. Wang, L.X. Zeng, Y.B. Chen, Z.Q. Liu, Dual-co-catalysts decorated rimous CdS spheres advancing highly-efficient visible-light photocatalytic hydrogen production, *Appl. Catal. B* 231 (2018) 101–107.
- [8] P.Y. Kuang, Y.Z. Su, K. Xiao, Z.Q. Liu, N. Li, H.J. Wang, J. Zhang, Double-shelled CdS and CdSe-cosensitized ZnO porous nanotube arrays for superior photoelectrocatalytic applications, *ACS Appl. Mater. Interfaces* 7 (2015) 16387–16394.
- [9] T. Giannakopoulou, I. Papailias, N. Todorova, N. Boukos, Y. Liu, J.G. Yu, C. Trapalis, Tailoring the energy band gap and edges' potentials of $\text{g-C}_3\text{N}_4/\text{TiO}_2$ composite photocatalysts for NOx removal, *Chem. Eng. J.* 310 (2017) 571–580.
- [10] Y.B. Liu, G.Q. Zhu, J.Z. Gao, M. Hojamberdiev, R.L. Zhu, X.M. Wei, Q.M. Guo, P. Liu, Enhanced photocatalytic activity of $\text{Bi}_4\text{Ti}_3\text{O}_{12}$ nanosheets by Fe^{3+} -doping and the addition of Au nanoparticles: photodegradation of phenol and bisphenol A, *Appl. Catal. B* 200 (2017) 72–82.
- [11] R. Vinoth, P. Karthik, C. Muthamizhchelvan, B. Neppolian, M. Ashokkumar, Carrier separation and charge transport characteristics of reduced graphene oxide supported visible-light active photocatalysts, *Phys. Chem. Chem. Phys.* 18 (2016) 5179–5191.
- [12] C.L. Yu, Z. Wu, R.Y. Liu, D. Dionysiou, K. Yang, C.Y. Wang, H. Liud, Novel fluorinated Bi_2MoO_6 nanocrystals for efficient photocatalytic removal of water organic pollutants under different light source illumination, *Appl. Catal. B* 209 (2017) 1–11.
- [13] X.M. Zhou, N. Liu, P. Schmuki, Photocatalysis with TiO_2 nanotubes: “colorful” reactivity and designing site-specific photocatalytic centers into TiO_2 nanotubes, *ACS Catal.* 7 (2017) 3210–3235.
- [14] S.K. Le, T.S. Jiang, Y.W. Li, Q. Zhao, Y.Y. Li, W.B. Fang, M. Gong, Highly efficient visible-light-driven mesoporous graphitic carbon nitride/ZnO nanocomposite photocatalysts, *Appl. Catal. B* 200 (2017) 601–610.
- [15] O. Tomita, T. Otsubo, M. Higashi, et al., Partial oxidation of alcohols on visible-light-responsive WO_3 photocatalysts loaded with palladium oxide cocatalyst, *ACS Catal.* 6 (2) (2016) 1134–1144.
- [16] S. Tokunaga, H. Kato, A. Kudo, Selective preparation of monoclinic and tetragonal BiVO_4 with scheelite structure and their photocatalytic properties, *Chem. Mater.* 13 (2001) 4624–4628.
- [17] J.H. Yao, H. Chen, F. Jiang, Z.Y. Jiao, M.C. Jin, Titanium dioxide and cadmium sulfide co-sensitized graphitic carbon nitride nanosheets composite photocatalysts with superior performance in phenol degradation under visible-light irradiation, *J. Colloid Interface Sci.* 490 (2017) 154–162.
- [18] C.L. Yu, G. Li, S. Kumar, K. Yang, R.C. Jin, Phase transformation synthesis of novel $\text{Ag}_2\text{O}/\text{Ag}_2\text{CO}_3$ heterostructures with high visible light efficiency in photocatalytic degradation of pollutants, *Adv. Mater.* 26 (2014) 892–898.

- [19] Q.Y. Chen, Y.F. Wang, Y.W. Wang, X.C. Zhang, D.H. Duan, C. Fan, Nitrogen-doped carbon quantum dots/Ag₃PO₄ complex photocatalysts with enhanced visible light driven photocatalytic activity and stability, *J. Colloid Interface Sci.* 491 (2017) 238–245.
- [20] D.H. Xia, T.H. An, G.Y. Li, W.J. Wang, H.J. Zhao, P.K. Wong, Synergistic photocatalytic inactivation mechanisms of bacteria by graphene sheets grafted plasmonic Ag-AgX (X = Cl, Br, I) composite photocatalyst under visible light irradiation, *Water Res.* 99 (2016) 149–161.
- [21] J. Chen, W.G. Mei, Q.J. Huang, N.A. Chen, C.L. Lu, H.J. Zhu, J. Chen, W.H. Hou, Highly efficient three-dimensional flower-like AgI/Bi₂O₃CO₃ heterojunction with enhanced photocatalytic performance, *J. Alloys Compd.* 688 (2016) 225–234.
- [22] X.Q. Yan, C. Xue, B.L. Yang, G.D. Yang, Novel three-dimensionally ordered macroporous Fe³⁺-doped TiO₂ photocatalysts for H₂ production and degradation applications, *Appl. Surf. Sci.* 394 (2017) 248–257.
- [23] B.C. Zhu, J.F. Zhang, C.J. Jiang, B. Cheng, J.G. Yu, First principle investigation of halogen-doped monolayer g-C₃N₄ photocatalyst, *Appl. Catal. B* 207 (2017) 27–34.
- [24] W.B. Li, C. Feng, S.Y. Dai, J.G. Yue, F.X. Hua, H. Hou, Fabrication of sulfur-doped g-C₃N₄/Au/CdS Z-scheme photocatalyst to improve the photocatalytic performance under visible light, *Appl. Catal. B* 168 (2015) 465–471.
- [25] F. Chen, Q. Yang, X.M. Li, G.M. Zeng, D.B.W.C.G. Niu, J.W. Zhao, H.X. An, T. Xie, Y.C. Deng, Hierarchical assembly of graphene-bridged Ag₃PO₄/Ag/BiVO₄ (040) Z-scheme photocatalyst: an efficient, sustainable and heterogeneous catalyst with enhanced visible-light photoactivity towards tetracycline degradation under visible light irradiation, *Appl. Catal. B* 200 (2017) 330–342.
- [26] F. Chen, Q. Yang, S.N. Wang, F.B. Yao, J. Sun, Y.L. Wang, C. Zhang, X.M. Li, C.G. Niu, D.B. Wang, G.M. Zeng, Graphene oxide and carbon nitride nanosheets co-modified silver chromate nanoparticles with enhanced visible-light photoactivity and anti-photocorrosion properties towards multiple refractory pollutants degradation, *Appl. Catal. B* 209 (2017) 493–505.
- [27] Y.Z. Hong, Y.H. Jiang, C.S. Li, W.Q. Fan, X. Yan, M. Yan, W.D. Shi, In-situ synthesis of direct solid-state Z-scheme V₂O₅/g-C₃N₄ heterojunctions with enhanced visible light efficiency in photocatalytic degradation of pollutants, *Appl. Catal. B* 180 (2016) 663–673.
- [28] H.L. Wang, L.S. Zhang, Z.G. Chen, J.Q. Hu, S.J. Li, Z.H. Wang, J.S. Liu, X.C. Wang, Semiconductor heterojunction photocatalysts: design, construction, and photocatalytic performances, *Chem. Soc. Rev.* 43 (2014) 5234–5244.
- [29] J. Zhang, Q. Xu, Z.C. Feng, M.J. Li, C. Li, Importance of the relationship between surface phases and photocatalytic activity of TiO₂, *Angew. Chem. Int. Ed.* 47 (2008) 1766–1769.
- [30] J.G. Hou, C. Yang, Z. Wang, W.L. Zhou, S.Q. Jiao, H.M. Zhu, In situ synthesis of α - β phase heterojunction on Bi₂O₃ nanowires with exceptional visible-light photocatalytic performance, *Appl. Catal. B* 142 (2013) 504–511.
- [31] Y.Y. Zhu, Y.F. Liu, Y.H. Lv, Q. Ling, D. Liu, Y.F. Zhu, Enhancement of photocatalytic activity for BiPO₄ via phase junction, *J. Mater. Chem. A* 2 (2014) 13041–13048.
- [32] W.K. Wang, J.J. Chen, X. Zhang, Y.X. Huang, W.W. Li, H.Q. Yu, Self-induced synthesis of phase-junction TiO₂ with a tailored rutile to anatase ratio below phase transition temperature, *Sci. Rep.* 6 (2016) 20491.
- [33] J. Cheng, J. Feng, W. Pan, Enhanced photocatalytic activity in electrospun bismuth vanadate nanofibers with phase junction, *ACS Appl. Mater. Interfaces* 7 (2015) 9638–9644.
- [34] Y. Kanigariidou, A. Petala, Z. Frontistis, M. Antonopoulou, M. Solakidou, I. Konstantinou, Y. Deligiannakis, D. Mantzavinos, D.I. Kondarides, Solar photocatalytic degradation of bisphenol A with CuOx/BiVO₄: insights into the unexpectedly favorable effect of bicarbonates, *Chem. Eng. J.* 318 (2017) 39–49.
- [35] M. Wang, Y.J. Shi, G.Q. Jiang, 3D hierarchical Zn₃(OH)₂V₂O₇·2H₂O and Zn₃(VO₄)₂ microspheres: synthesis, characterization and photoluminescence, *Mater. Res. Bull.* 47 (2012) 18–23.
- [36] S.W. Cao, Y. Li, B.C. Zhu, M. Jaroniec, J.G. Yu, Facet effect of Pd cocatalyst on photocatalytic CO₂ reduction over g-C₃N₄, *J. Catal.* 349 (2017) 208–217.
- [37] B.C. Zhu, P.F. Xia, Y. Li, W.K. Ho, J.G. Yu, Fabrication and photocatalytic activity enhanced mechanism of direct Z-scheme g-C₃N₄/Ag₂WO₄ photocatalyst, *Appl. Surf. Sci.* 391 (2017) 175–183.
- [38] A.Y. Meng, B.C. Zhu, B. Zhong, L.Y. Zhang, B. Cheng, Direct Z-scheme TiO₂/CdS hierarchical photocatalyst for enhanced photocatalytic H₂-production activity, *Appl. Surf. Sci.* (2017).
- [39] M.N. Subramaniam, P.S. Goh, N. Abdullah, W.J. Lau, B.C. Ng, A.F. Ismail, Adsorption and photocatalytic degradation of methylene blue using high surface area titanate nanotubes (TNT) synthesized via hydrothermal method, *J. Nanopart. Res.* 19 (2017) 220.
- [40] D.F. Xu, Y. Hai, X.C. Zhang, S.Y. Zhang, R.G. He, Bi₂O₃ cocatalyst improving photocatalytic hydrogen evolution performance of TiO₂, *Appl. Surf. Sci.* 400 (2017) 530–536.
- [41] Z.Z. Wu, X.Z. Yuan, H. Wang, Z.B. Wu, L.B. Jiang, H. Wang, L. Zhang, Z.H. Xiao, X.H. Chen, G.M. Zeng, Facile synthesis of a novel full-spectrum-responsive Co₂.67S₄ nanoparticles for UV-, vis- and NIR-driven photocatalysis, *Appl. Catal. B* 202 (2017) 104–111.
- [42] J. Tian, R.Y. Liu, Z. Liu, C.L. Yu, M.C. Liu, Boosting the photocatalytic performance of Ag₂CO₃ crystals in phenol degradation via coupling with trace N-QDs, *Chin. J. Catal.* 38 (2017) 1999–2008.
- [43] X.L. Hu, Y.Y. Li, J. Tian, H.R. Yang, H.Z. Cui, Highly efficient full solar spectrum (UV-vis-NIR) photocatalytic performance of Ag₂S quantum dot/TiO₂ nanobelt heterostructures, *J. Ind. Eng. Chem.* 45 (2017) 189–196.
- [44] Y.C. Huang, W.J. Fan, B. Long, H.B. Li, F.Y. Zhao, Z.L. Liu, Y.X. Tong, H.B. Ji, Visible light Bi₂S₃/Bi₂O₃/Bi₂O₃CO₃ photocatalyst for effective degradation of organic pollutants, *Appl. Catal. B* 185 (2016) 68–76.
- [45] L.L. Zhang, Z.P. Xing, H. Zhang, Z.Z. Li, X.Y. Wu, X.D. Zhang, Y. Zhang, W. Zhou, High thermostable ordered mesoporous SiO₂-TiO₂ coated circulating-bed biofilm reactor for unpredictable photocatalytic and biocatalytic performance, *Appl. Catal. B* 180 (2016) 521–529.
- [46] L.Q. Jing, Y.G. Xu, S.Q. Huang, M. Xie, M.Q. He, H. Xu, H.M. Li, Q. Zhang, Novel magnetic CoFe₂O₄/Ag/Ag₃VO₄ composites: highly efficient visible light photocatalytic and antibacterial activity, *Appl. Catal. B* 199 (2016) 11–22.
- [47] S.M. Wang, Y. Guan, L.P. Wang, W. Zhao, H. He, J. Xiao, S.G. Yang, Sun C, Fabrication of a novel bifunctional material of BiOI/Ag₃VO₄ with high adsorption-photocatalysis for efficient treatment of dye wastewater, *Appl. Catal. B* 168 (2015) 448–457.
- [48] L.L. Yang, Y.W. Tang, L.P. Tong, H. Zhou, J. Ding, T.X. Fan, D. Zhang, Efficient visible light photocatalytic water oxidation on Zn₃(OH)₂V₂O₇·2H₂O nanoplates: effects of exposed facet and local crystal structure distortion, *Appl. Surf. Sci.* 346 (2015) 115–123.
- [49] H.J. Kong, D.H. Won, J. Kim, S.I. Woo, Sulfur-doped g-C₃N₄/BiVO₄ composite photocatalyst for water oxidation under visible light, *Chem. Mater.* 28 (2016) 1318–1324.
- [50] S.N. Gu, W.J. Li, F.Z. Wang, H.D. Li, H.L. Zhou, Substitution of Ce (III, IV) ions for Bi in BiVO₄ and its enhanced impact on visible light-driven photocatalytic activities, *Catal. Sci. Technol.* 6 (2016) 1870–1881.
- [51] M. Jeem, L.H. Zhang, J.Y. Ishioka, T. Shibayama, T. Iwasaki, T. Kato, S. Watanabe, Tuning optoelectrical properties of ZnO nanorods with excitonic defects via submerged illumination, *Nano Lett.* 17 (2017) 2088–2093.
- [52] Y.B. Yan, Y.L. Yu, D. Wu, Y.J. Yang, Y.A. Cao, TiO₂/vanadate (Sr₁₀V₆O₂₅, Ni₃V₂O₈, Zn₂V₂O₇) heterostructured photocatalysts with enhanced photocatalytic activity for photoreduction of CO₂ into CH₄, *Nanoscale* 8 (2016) 949–958.
- [53] L.X. Pang, D. Zhou, Z.M. Qi, W.G. Liu, Z.X. Yue, I.M. Reaney, Structure-property relationships of low sintering temperature scheelite-structured (1-x) BiVO₄-xLaNbO₄ microwave dielectric ceramics, *J. Mater. Chem. C* 5 (2017) 2695–2701.
- [54] S.B. Ni, T. Li, X.L. Yang, Synthesis of Co₃(OH)₂V₂O₇·1.7H₂O nanosheets and its application in lithium ion batteries, *Mater. Lett.* 63 (2009) 2459–2461.
- [55] S.B. Ni, X.H. Wang, G. Zhou, F. Yang, J.M. Wang, D.Y. He, Crystallized Zn₃(VO₄)₂: synthesis, characterization and optical property, *J. Alloys Compd.* 491 (2010) 378–381.
- [56] D. You, H. Fukuzawa, Y. Sakakibara, T. Takanashi, Y. Ito, G.G. Maliyar, K. Motomura, K. Nagaya, T. Nishiyama, K. Asa, Y. Sato, N. Saito, M. Oura, M. Schöfke, G. Kastirke, U. Hergenhanh, V. Stumpf, K. Gokhberg, A.I. Kuleff, L.S. Cederbaum, K. Ueda, Charge transfer to ground-state ions produces free electrons, *Nat. Commun.* 8 (2017) 14277.
- [57] C. Reitz, B. Breitung, A. Schneider, D. Wang, M.V.D. Lehr, T. Leichtweiss, J. Janek, H. Hahn, T. Brezesinski, Hierarchical carbon with high nitrogen doping level: a versatile anode and cathode host material for long-life lithium-ion and lithium-sulfur batteries, *ACS Appl. Mater. Interfaces* 8 (2016) 10274–10282.
- [58] H.B. Li, Y.F. Qiao, J. Li, H.L. Fang, D.H. Fan, W. Wang, A sensitive and label-free photoelectrochemical aptasensor using Co-doped ZnO diluted magnetic semiconductor nanoparticles, *Biosens. Bioelectron.* 77 (2016) 378–384.
- [59] H. Alhummany, S. Rafique, K. Sulaiman, XPS analysis of the improved operational stability of organic solar cells using a V₂O₅ and PEDOT: PSS composite layer: effect of varied atmospheric conditions, *J. Phys. Chem. C* 121 (2017) 7649–7658.
- [60] D.D. Tang, G.K. Zhang, Ultrasonic-assistant fabrication of cocoon-like Ag/AgFeO₂ nanocatalyst with excellent plasmon enhanced visible-light photocatalytic activity, *Ultrason. Sonochem.* 37 (2017) 208–215.
- [61] P.Y. Kuang, P.X. Zheng, Z.Q. Liu, J.H. Lei, H. Wu, N. Li, T.Y. Ma, Embedding Au quantum dots in rimous cadmium sulfide nanospheres for enhanced photocatalytic hydrogen evolution, *Small* 12 (2016) 6735–6744.
- [62] H.B. Zeng, Z.G. Li, W.P. Cai, B.Q. Cao, P.S. Liu, S.K. Yang, Microstructure control of Zn/ZnO core/shell nanoparticles and their temperature-dependent blue emissions, *J. Phys. Chem. B* 111 (2007) 14311–14317.
- [63] N. Zhang, M.Q. Yang, Z.R. Tang, Y.J. Xu, Toward improving the graphene-semiconductor composite photoactivity via the addition of metal ions as generic interfacial mediator, *ACS Nano* 8 (2014) 623–633.
- [64] M.S. Ren, J.M. Song, Y.L. Shi, Y.B. Xiang, G. Hu, Synthesis of zinc pyrovanadate 3D flower-like microspheres and their photocatalytic properties, *J. Cryst. Growth* 402 (2014) 119–123.
- [65] Y.Y. Zhu, Y.J. Wang, Q. Ling, Y.F. Zhu, Enhancement of full-spectrum photocatalytic activity over BiPO₄/Bi₂WO₆ composites, *Appl. Catal. B* 200 (2017) 222–229.
- [66] M. Yan, Y.Q. Hua, F.F. Zhu, W. Gu, J.H. Jiang, H.Q. Shen, W.D. Shi, Fabrication of nitrogen doped graphene quantum dots-BiOI/MnNb₂O₆ pn junction photocatalysts with enhanced visible light efficiency in photocatalytic degradation of antibiotics, *Appl. Catal. B* 202 (2017) 518–527.
- [67] R.B. Wei, P.Y. Kuang, H. Cheng, Y.B. Chen, J.Y. Long, M.Y. Zhang, Z.Q. Liu, Plasmon-enhanced photoelectrochemical water splitting on gold nanoparticle decorated ZnO/CdS nanotube arrays, *ACS Sustain. Chem. Eng.* 5 (2017) 4249–4257.
- [68] Y.C. Rui, H. Xiong, B. Su, H.Z. Wang, Q.H. Zhang, J.L. Xu, P. Müller-Buschbaum, Liquid-liquid interface assisted synthesis of SnO₂ nanorods with tunable length for enhanced performance in dye-sensitized solar cells, *Electrochim. Acta* 227 (2017) 49–60.
- [69] J.W. Zhang, G. Cao, H.Y. Wang, P.Z. Feng, Z.S. Liu, Graphene-Bi₂₄O₃₁Br₁₀ composites with tunable architectures for enhanced photocatalytic activity and mechanism, *Ceram. Int.* 42 (2016) 11796–11804.
- [70] C.B.D. Maric, C. Marchal, A. Koch, D. Robert P. Drogui, Sol-gel synthesis of TiO₂ nanoparticles: effect of Pluronic P123 on particle's morphology and photocatalytic degradation of paraquat, *Environ. Sci. Pollut. Res.* 24 (2017) 12582–12588.
- [71] J. Di, J. Chen, M.X. Ji, Q. Zhang, L. Xu, J.X. Xia, H.M. Li, Reactable ionic liquid

- induced homogeneous carbon superdoping of BiPO₄ for superior photocatalytic removal of 4-chlorophenol, *Chem. Eng. J.* 313 (2017) 1477–1485.
- [72] F.L. Liao, Z.Y. Zeng, C. Eley, Q. Lu, X.L. Hong, S.C.E. Tsang, Electronic modulation of a copper/zinc oxide catalyst by a heterojunction for selective hydrogenation of carbon dioxide to methanol, *Angew. Chem. Int. Ed.* 51 (2012) 5832–5836.
- [73] S. Singh, R. Sharma, G. Joshi, J.K. Pandey, Formation of intermediate band and low recombination rate in ZnO-BiVO₄ heterostructured photocatalyst: investigation based on experimental and theoretical studies, *Korean J. Chem. Eng.* 34 (2017) 500–510.
- [74] H.X. Guo, D. Guo, Z.S. Zheng, W. Wen, Hydrothermal synthesis and visible light photocatalytic activities of Zn₃(VO₄)₂ nanorods, *J. Mater. Res.* 29 (2014) 2934–2941.
- [75] S.D. Abraham, S.T. David, R.B. Bennie, C. Joel, M. Seethalakshmi, T. Adinaween, Microwave assisted synthesis, characterization and photocatalytic activity of Zn₂V₂O₇ nanospheres, *Chem. Sci. Trans.* 3 (2014) 1488–1496.
- [76] J.P. Wang, Z.Y. Wang, B.B. Huang, Y.D. Ma, Y.Y. Liu, X.Y. Qin, X.Y. Zhang, Y. Dai, Oxygen vacancy induced band-gap narrowing and enhanced visible light photocatalytic activity of ZnO, *ACS Appl. Mater. Interfaces* 4 (2012) 4024–4030.
- [77] E.P. Gao, W.Z. Wang, M. Shang, J.H. Xu, Synthesis and enhanced photocatalytic performance of graphene-Bi₂WO₆ composite, *Phys. Chem. Chem. Phys.* 13 (2011) 2887–2893.